JPRS-CST-91-002
16 JANUARY 1991

JPRS Report

Science & Technology

China

Science & Technology
China

JPRS-CST-91-002

CONTENTS

16 January 1991

SCIENCE & TECHNOLOGY POLICY

DEFENSE R&D

ADVANCED MATERIALS

BIOTECHNOLOGY

COMPUTERS

FACTORY AUTOMATION, ROBOTICS

LASERS, SENSORS, OPTICS

MICROELECTRONICS

PHYSICS

Intellectual Rights Must Be Protected

91FE0204B Beijing CHINA DAILY in English
13 Dec 90 p 4

[Text] If wealth referred mainly to land in ancient times and machines in modern times, it lies largely in intellectual achievements in today's society.

In fact, the protection of intellectual property has become a major concern in China.

The nation's legislative body, the National People's Congress, has approved three laws involving intellectual property, on patent, trademark, and copyright in recent years.

In the hope of promoting the upgrading of domestic technology and international trade and co-operation three senior scholars discussed the different perspectives on the protection of intellectual property in China during a recent interview with GUANGMING DAILY.

When the highly centralized national economy first broke out of the Soviet model and showed an interest in foreign technology and investment, it faced an overwhelming demand for legislation meant to safeguard intellectual property.

When the nation's lawmakers set out to draft the patent law in 1979, opinions differed alarmingly, according to Tang Zongshun, consultant to the State Council and vice-chairman of the China branch of the International Association for Intellectual Property Protection.

Some people insisted that socialist enterprises should not adopt patents. Still others held that the making of a patent law would largely benefit foreigners because there were fewer inventions in China.

But all those worries have proved unnecessary, Tang said.

While providing protection for patent owners, the law has also allowed the government to co-ordinate domestic patent affairs. This administrative power is expected to prevent monopolies of technology while safeguarding patent ownership, according to Tang.

To the lawmakers' surprise, the law has stirred up unprecedented enthusiasm for the introduction of inventions and technical innovations throughout the country.

It is at the same time a strong incentive for foreigners who previously maintained a wait-and-see attitude due to the lack of patent protection in the Chinese market. More and more foreign firms have been attracted to the country, bringing funds as well as technology.

However, Tang said, the nation has to do more to catch up with advanced countries in this field. Now that the nation is attempting to adopt international standards, it must make immediate efforts to narrow the gap.

Many countries regularly revise their legislation to keep in step with international progress.

But in China it takes several years from the initial drafting to the adoption of a new law. Meanwhile, laws are not adequately enforced.

There are three departments in charge of patent, trademark and copyright protection in China. All such affairs are under just one agency in many other countries. Considerable inconvenience has resulted in the field of international co-operation as a result of differences in the systems, Tang complained.

In actual fact, he said, some protective measures regarding the nation's foreign trade are no different from the international conventions—only administrative protection has to be replaced with legal means.

Despite the existing laws concerning intellectual property, the violation of property rights is still rife. Hence the question now is how to enforce the laws effectively, Tang said.

With foreign trade increasing, there have been more and more complaints and inquiries from the foreign side involving the three laws. Meanwhile, there have been international treaties which involve two or more kinds of intellectual property.

The country might suffer economic losses if its different departments in charge of intellectual property produce conflicting answers to the same questions, according to Zheng Chengsi, a research fellow with the Chinese Academy of Social Sciences and director of the China branch of the International Association of Industrial Property Rights Protection.

There must also be proper co-ordination in the making, revision and explanation of laws in order to eliminate conflicts, Zheng appealed.

There are some widely-accepted principles in the field of international intellectual property protection. Every country strives to obtain the greatest benefit within the limits of international conventions. This seems even more imperative in China's case, Zheng said.

China has done more than its laws have promised in protecting intellectual property. For example, the patent law does not acknowledge the international convention that patent owners enjoy the right to ban others from importing the same products as theirs. This has been criticized by foreigners as violation of international conventions. But in fact, the patent law bestows on patent owners the right to prohibit others from using, or selling, their products. This is no different from prohibiting others from importing the same products. Therefore, Zheng said, the disregard of the convention is merely nominal in the law. The problem can be solved easily through a slight rewording.

Guo Shoukang, professor of law and chairman of the Intellectual Property Protection Teaching and Research

Centre of the Chinese People's University, called for more detailed regulations and stricter enforcement of the existing laws.

Soviet Link to Aid Ocean Studies

91FE0204A Beijing CHINA DAILY in English 23 Nov 90 p 1

[Article by Wang Rong]

[Text] China's drive in promoting international co-operation in oceanic studies is to enter a new phase next year when Chinese oceanologists start working with their Soviet counterparts for the first time.

The contracts for several co-operation projects in the area will be finalized next May when a group of Soviet delegates come to Beijing, according to Yan Hongmo, director of the State Oceanic Administration (SOA).

The contracts are the result of a bilateral agreement on co-operation in oceanic studies for peaceful purposes which are signed in September in Moscow by the SOA and the Soviet State Committee for Science and Technology.

The agreement made the Soviet Union the SOA's ninth partner in oceanic studies for peaceful purposes, following the United States, Germany, Japan, the Democratic People's Republic of Korea and four Latin American countries, Yan said.

He said China and the Soviet Union would co-operate in a wide range of fields, from marine physics and geology to information exchange and instrument development. Co-operation would follow the principles laid down by the agreement, which was valid for five years.

Sino-Soviet co-operation, he said, was based on the mutual interest in study of the western part of the North Pacific which both countries bordered in the east, and of the Kuroshio, a northward-moving warm current originating in waters near the tropics and heading into the Japan Sea.

Yan said the two countries could complement each other in marine study.

China engaged mainly in the study of coastal waters, he said, and could learn from the Soviet Union's oceanic research in geological structure, marine surveys, charting, marine resources utilization and environmental protection. The country's wealth of oceanic information would also be useful.

On the other hand, he said, the Soviet Union could profit from China's updated instruments, data processing techniques and marine exploration technology.

Meanwhile, Yan said the SOA was expecting its 10th foreign partner—France—from ongoing negotiations between the two countries.

"Oceanology can't do without exchange," he said. "And China is willing to co-operate with other countries in pioeering and global oceanic studies, especially those bordering the western part of the North Pacific."

Tank Simulator Offers High-Tech Target Practice

40100019 Beijing CHINA DAILY in English
18 Dec 90 p 5

[Article by Li Sheng]

[Text] Looking through a telescope with your right hand holding on to a firing control gear, operating the TCM-1 tank firing simulator is very much like playing a video game.

You feel as if you are in the real thing as you try to aim and fire at the moving targets while sitting in a tilting chair, listening to the gunfire.

Designed by the Beijing Special Vehicle Research Institute, the new TCM-1 is used to train the tank turret crew in the handling of turret controls and firing procedures. Equipped with the latest laser and computer technology, it has reached the level of advanced international tank simulators.

The tank's elevation, deflection and other control gears are realistically simulated to allow trainees to practise tracking, aiming and firing at moving as well as stationary targets.

The TCM-1 is an improved version of TSM-2. Both are used for firing training of T-59, T-69, T-54 and T-54A tank gunners, but with slight modifications, they can be used for other types of tanks and guns.

The TSM-2 only takes one gunner at a time for firing practice, while the more sophisticated TCM-1 can provide teamwork training for the whole turret crew—commander, gunner and loader.

According to Liao Wenliang, the head of the research group for the tank simulators, 15 TSM-2s have been put into use in Chinese army units or schools in the past 3 years and they have been well received because of their relatively low cost and high degree of realism.

Training on the TSM-2 costs only 1/270th as much as in a real vehicle, while on the new TCM-1 the cost is 1/2,500th of what the cost would be in a real tank, Liao said. Because of limited funds, a tank gunner can only expect to fire four to six shells during his 2 or 3 years of army service. But tank simulators can provide adequate training at an affordable price, Liao said. In 1987, two groups of gunners were trained separately on the TSM-2s and the real tanks for a month and there was not a significant difference in their results.

Last year the TSM-2 won a first-class award for military technical achievement. This year it has been exported on the international market at a price of $150,000. The export model has adopted a new control system, which has greatly improved the machine's reliability and applications.

More realistic and flexible, the new TCM-1 model is also available for export now at a price of $500,000. Instead of using ready-made slide pictures, it uses a laser disc to store and produce a firing drill background in front of the telescope and its computer creates targets that can move against the background and imitate being fired at with life-like sounds and images.

The commander on the TCM-1 can observe the target area through a periscope and give orders to loaders and gunners. The crew can feel the simulated barrel recoil and its vibration just as in a real tank.

World-Record Magnetic Energy Product for Nd-Fe-B Magnet Material

91P60066A Beijing KEJI RIBAO [SCIENCE AND TECHNOLOGY DAILY] in Chinese 6 Dec 90 p 1

[Article by Hu Zuo [5170 1563]: "Baotou Neodymium-Iron-Boron Permanent-Magnet Material's Magnetic Energy Product Sets World Record"]

[Summary] Hohhot, 4 Dec—It has been learned from the Baotou Rare-Earth Research Institute (BREI) that—as verified the other day by the China Institute of Metrology—the magnetic energy product of the NdFeB permanent-magnet material developed by BREI has reached a value of 415 KJ/m^3 (52.2 megagauss-oersteds), surpassing the previously reported world record of 402 KJ/m^3 (50.6 megagauss-oersteds) set by Japanese researchers.

Over the past three years, 52-year-old scientist Xie Hongzu [6200 1347 4371] and his three approximately 30-year-old assistants, using domestically developed and manufactured equipment, have perfected a low-oxygen-supply technique for industrial-scale production of the material. In their experiments, all of the samples had a magnetic energy product of 390 KJ/m^3 or higher, with the best attaining the aforementioned value of 415 KJ/m^3. BREI will begin industrial-scale production of the material next year [i.e., 1991].

Studies on the Synthetic Method of 2', 3'-Dideoxynucleosides

40091004N Chengdu SICHUAN DAXUE XUEBAO [JOURNAL OF SICHUAN UNIVERSITY—NATURAL SCIENCE EDITION] in Chinese Vol 27 No 4, Nov 90 p 478

[Article by Li Yingfu [2621 5391 1381] and Yi Changhou [1707 2490 0624], Department of Chemistry]

[Abstract] A new synthetic route of 2', 3'-dideoxynucleosides which are now being clinically evaluated as treatment against AIDS is suggested and the synthetic method of the dideoxynue-leosides prepared with tetrahydrofurfuryl alcohol as the starting material is reported. High optical purity (greater than 90 percent) (S)-Tetrahydrofurfuryl acetate was successfully obtained by the optical resolution of (plus or minus)-tetrahydrofurfuryl alcohol with D-camphor-10-sulforyl chloride. The radical chlorination of tetrahydrofurfuryl acetate was investigated by use of ^{1}H-NMR and 5-o-acetyl-2, 3-dideoxypentofuyanoyl chloride, a new important intermediate prepared 2', 3'- dideoxynucleosides, was synthesised. For the intermediate, the effects of changes in reaction time, temperature and mole ration of reactants on the reaction products were determined, the optimum conditions of the reaction were obtained and the yield of 5-o-acetyl-2, 3-pentfaranoyl chloride could be increased up to 50 percent from 10 percent. The possibility of the further condensation with the bases of nucleosides was also discussed.

Comparison of Three Methods for Screening Aflatoxin-Producing Strains

40091004M Beijing ZHONGHUA YUFANG YIXUE ZAZHI [CHINESE JOURNAL OF PREVENTIVE MEDICINE] in Chinese Vol 24 No 5, Sep 90 p 289

[Article by Wang Zhigang [3769 1807 0474], Tong Zhe [4547 5764], et al.; Zhejiang Institute of Food Safety Control and Inspection, Hangzhou]

[Abstract] By using rice medium microcolumn method, aflatoxin-producing ability medium dish method (APA method), A and M medium thin-layer chromato scanner method (AM method), 76 strains of Aspergillus flavus from the foodstuffs in Zhejiang province were screened for aflatoxin-producing strains, and which were confirmed with thin-layer chromatography method. Using the above three methods, aflatoxin-producing strains rates were detected respectively in 11.8 percent, 9.2 percent and 18.4 percent. Twenty aflatoxigenic strains were determined positive by all three methods (26.3 percent). All three methods showed false negatives. The AM method and APA method both showed false positives. The causes of false negatives and positives were discussed and the accord-rate of AM method with other methods was the highest as compared with that of microcolumn or APA method. False positives appeared in both APA method and AM method. The causes of false negative and positive were discussed. It was suggested that AM method be a safe, simple, and reliable method for screening aflatoxigenic strains.

The Natural Infection Rate of Mosquitoes by Japanese Encephalitis B Virus in Yunnan Province

40091004L Beijing ZHONGHUA YUFANG YIXUE ZAZHI [CHINESE JOURNAL OF PREVENTIVE MEDICINE] in Chinese Vol 24 No 5, Sep 90 p 267

[Article by Zhang Halin [1728 3189 2651], Zi Dengyun [5261 4098 0061, et al.; Yunnan Provincial Institute for Control and Research of Epidemic Diseases, Dali]

[Abstract] In July-September 1983-1987, 57,898 adult female mosquitoes belonging to 29 species of 8 genera were collected from Japanese B encephalitis (JE) epidemic areas in Yunnan, China, and were examined by C 6/36 cell method and sucking mouse method. Twenty-eight strains of JE virus were isolated from Culex tritaeniorhychus, C. whitomorei, C. pseudovishnui, C. fuscocephala, C. annulus, C. gelidus, Anopheles sinensis, Mansonia uniformis, Aedes albopictus, Ae. Vexans, Ae. lineatopennis, and Ae. assamensis. The positive isolation rates by the two methods were 6.19 percent and 3.33 percent respectively. The highest positive isolation rate 12.3 percent (per 100 pools), mosquito body virus carrier rate 1208 or mosquito body virus carrier rate 4.81 percent (per 1000 mosquitoes) were found in the middle 10 days of August, corresponding to epidemic peak of JBE Nine strains of JE virus were isolated from C tritaeniorhynchus with an isolation rate of 7.44 percent natural isolation ratio was 2.584 percent and mosquito body virus carrier rate 1.71 percent. These results indicated that C. tritaeniorhynchus might be the main vector of JE virus in Yunnan, while C. whitmorei, C. pseudovishnui and An. sinensis are also important vectors of JE virus in Yunnan.

Study on Natural Infection of Epidemic Haemorrhagic Fever Virus in Leptotrombidium scutellare

40091004K Beijing ZHONGHUA YUFANG YIXUE ZAZHI [CHINESE JOURNAL OF PREVENTIVE MEDICINE] in Chinese Vol 24 No 5, Sep 90 p 263-264

[Article by Zhang Yun [1728 0061], Dou Rui [4535 5605], et al.; Institute of Military Medicine PLA, Nanjing]

[Abstract] Leptotrombidium (L.) scutellare was considered to be the suspected vector of epidemic haemorrhagic fever (EHF). In order to clarify the relationship between this mite and EHF, from October to November 1988 and October of 1989, the larvae of this mite were collected from rats in areas with constantly high incidence of EHF in Shanxi Province and larvae with only a small quantity of meal were selected and stored for more than 15 days before isolation of EHFV. Six strains of

virus were isolated. The virus isolated were identified to be EHFV by serum test, immunofluorescent blocking test as well as neutralization test. The above results further demonstrate this mite can naturally be infected by EHFV and therefore serve as vector of EHF.

Survey of Bacillus thuringiensis and Bacillus sphaericus from Soils of Four Provinces of China and Their Principal Biological Properties

40091004J Beijing WEISHENGWU XUEBAO [ACTA MICROBIOLOGICA SINICA] in Chinese Vol 30 No 5, Oct 90 p 388

[Article by Li Rongsen [2621 2837 2773], Dai Shunying [2071 7311 5391], et al.; Wuhan Institute of Virology, Academia Sinica, Wuhan]

[Abstract] A number of isolates of Bacillus thuringiensis and Bacillus sphaericus were obtained from soils of Southwestern Area and Shaanxi Province of China. Among isolates of B. thuringiensis were under 13 sorts of serotype in total of 23 sorts of B. thuringiensis and about 20 percent of auto-agglutinate strains. Rules of ecologic distribution of two sorts of bacteria were analysed. Toxicities on six species of insects, morphology and crystal proteins of B. thuringiensis, as well as toxicities, morphology and crystal proteins of B. sphaericus, were investigated. Twenty-two strains of more efficient of B. thuringiensis and 2 strains of more efficient of B. sphaericus were obtained. It was shown that B. thuringiensis is actually soil microorganism, and resource of B. thuringiensis is much fruitful in Southwestern Area of China.

Enzyme-Linked Immunosorbent Assay of Larvicidal Toxic Proteins of Bacillus Sphaericus Ts-1

40091004I Beijing WEISHENGWU XUEBAO [ACTA MICROBIOLOGICA SINICA] in Chinese Vol 30 No 5, Oct 90 p 374

[Article by Wang Jian [3769 0256], Ren Gaixin [0117 2395 2450], and Shang Kejin [1424 0344 6651]; Department of Biology, Nankai University, Tianjin]

[Abstract] Bacillus sphaericus Ts-1 Mosquito larvicidal toxins 42 k Da and 43 k Da were isolated by Sephadex G-200 chromatography. Three strains of highly toxic B. sphaericus and two nontoxic strains were screened for toxic proteins using ELISA. The lowest detectable toxin level was 1.56 X 10^{-5} mg/ml. Nontoxic strains did not produce antigens reacting to either the 42 kDa or the 43 kDa antibodies.

Ts-1 cultures were examined at 12 h and 24 h and LC_{50} bioassay against Culex pipiens. The C_{50}'s at 12 h and 24 h were 0.71 ppm and 0.154 ppm, respectively, the toxin level at 24 h was 4.6 times the level at 12 h. ELISA tests established total toxin at 0.049 mg/ml and 0.225 mg/ml at 12 h and 24 h, respectively, confirming the LC_{50} study.

The Location of Nodulation Genes in Rhizobium Astragali

40091004H Beijing WEISHENGWU XUEBAO [ACTA MICROBIOLOGICA SINICA] in Chinese Vol 30 No 5, Oct 90 p 335

[Article by Wei Hui [7614 6540], Wuhan Institute of Virology, Academia Sinica, Wuhan; Li Fudi [2621 7079 2769], Huazhong Agricultural University, Wuhan]

[Abstract] Based on the conservation of nod ABC genes in Rhizobium, authors located the nodulation genes on the plasmids of Rhizobium astragali. Both plasmid pRa7653Ra and plasmid pRa7653Rb carried nod genes in strain 7653R. Only plasmid pRa52a carried nod genes in strain S52. In strain SR72, the nod genes were harbored exclusively on plasmid pRa72a, the BamHI, HindIII and PstI fragments contained nod ABC genes were 22.4 kb, 11.9 kb and 2.2 kb respectively; the EcoRl fragments were 4.6 kb and 3.0 kb. In strain HR104, the nod genes were harbored exclusively on plasmid pRa104a, the BamHl, EcoRl and Pstl fragments contained nod ABC genes were 22.4 kb, 9.1 kb and 2.2 kb respectively.

Construction of Frankia Genomic Libraries and Isolation of Clones Homologous to Nodulation Genes from Rhizobium leguminosarum

40091004G Beijing YICHUAN XUEBAO [ACTA GENETICA SINICA] in Chinese Vol 17 No 5, Oct 90 p 410

[Article by Cui Yuhai, Qin Min, et al.; Laboratory of Molecular Genetics, Guangxi Agricultural College, Nanning—Project supported by the National Natural Science Foundation of China]

[Abstract] High molecular genomic DNAs were isolated by using the lysozyme plus achromopeptidase system from Frankia strains At4, Ccol and Hr16, the root nodule endophytes of Alnus, Casuarina and Hippophae respectively, and used to construct genomic libraries in pLAFRl, a broad host range cosmid vector within many gram-negative hosts. The genomic libraries were screened by in situ colony hybridization to identify clones homologious to common nodulation genes of Rhizobium leguminosarum, based on the sequence homology of EcoRI-digested Frankia total DNA to nod ABC from Rhizobium meliloti. Several clones showing relatively strong hybridization were found, the recombinant plasmid was isolated, and their homology with Rhizobium nodulation genes was confirmed by spot hybridization. Further work on these positive clones is now underway.

Stability and Gene Expression of Foreign Plasmid in Bacillus subtilis BF7658

40091004F Beijing YICHUAN XUEBAO [ACTA GENETICA SINICA] in Chinese Vol 17 No 5, Oct 90 p 404

[Article by Geng Yunqi [5105 6663 3825], Jiang Ruzhang [5592 1172 3864], and Li Jun [2621 7165]; Laboratory of Biotechnology, Department of Biology, Nankai University, Tianjin]

[Text] The plasmid pAmy411 carrying thermostable α-amylase gene has been transduced into B. subtilis BF7658 by bacteriophage PBS1. The transduction frequency was 10^{-9} transductants per PFU. The stability of plasmid pAmy411 in B. subtilis BF7658 was lower than that in B. subtilis AS1.1176, whereas the copy numbers were double than that in B. subtilis AS1.1176. The expressive level of thermostable α-amylase gene was about 6 times higher than that in B. subtilis AS1.1176.

Cloning and Expression of E. coli Glucose Isomerase Gene in Streptomyces lividans

40091004E Beijing YICHUAN XUEBAO [ACTA GENETICA SINICA] in Chinese Vol 17 No 5, Oct 90 p 397

[Article by Tan Huarong [6223 5478 2837], He Song [0149 2646], Zhuang Zenghui [8369 1073 6540], Xue Yugu [5641 4416 6253]; Institute of Microbiology, Academia Sinica, Beijing and Zhang Qijiu [1728 0366 3773]; Institute of Biophysics, Academia Sinica, Beijing]

[Abstract] E. coli glucose isomerase gene was cloned into Streptomyces lividans using shuttle plasmid vector pSE-3. First plasmid pX1203 was constructed in E. coli using plasmids pX1200 (containing 1.6 kb glucose isomerase gene) and pGEM-3 digested with EcoR1. Then, recombinant plasmid pSEX100 was also constructed in E. coli using plasmids pX1203 and pSE-3 digested with HindIII. When the pSEX100 was transformed into Streptomyces lividans protoplasts, recombinants were obtained on R5YE medium containing 50 μg/ml neomycin and 50 μg/ml thiostrepton.

The results showed that the E. coli glucose isomerase gene cloned and expressed in Streptomyces lividans via the analysis of restriction enzyme digestion as well as the detection of the glucose isomerase activity.

Location of the PSIIP680 ChlaAP Gene in the Chloroplast Genome of Rice

40091004D Beijing YICHUAN XUEBAO [ACTA GENETICA SINICA] in Chinese Vol 17 No 5, Oct 90 p 382

[Article by Zhu Jiahui [2612 0857 2547], Li Jigeng [2621 4949 5087, and Kong Fanrui [1313 4907 3843]; Institute of Genetics, Academia Sinica, Beijing]

[Abstract] A simple method for the preparation of chloroplast DNA (ctDNA) from rice has been developed. The rice ctDNA prepared with this method has successfully been used in restriction enzyme mapping anl Southern transfer. The gene probe of PSIIP680ChlaAP from spinach was hybridized with Pst-1, Pst-14, Pvu-2 and Sal-1 fragments of rice ctDNA in Southern hybridization. According to the physical map of rice ctDNA drawn by Hirai and Zhao Yan, this gene located at the site nearby the RuBPCase LS gene and about 26 kb from the nearer one of the inverted repeat region in the chloroplast genome of rice. The arrangement pattern of these genes was observed in chloroplast genome in higher plants for the first time.

Construction of a Gene Library and Screening of the Growth Hormone Gene from Sheep

40091004C Shanghai SHENGWUHUAXUE YU SHENGWUWULI XUEBAO [ACTA BIOCHIMICA et BIOPHYSICA SINICA] in Chinese Vol 22 No 5, Sep 90 p 496

[Article by Ren Zhaojun [0117 0340 6874], Shanghai Institute of Biochemistry, Academia Sinica; Feng Qihui [7458 03666546], South China Agriculture University; Shen Xiaozhou [3088 1321 1352], Institute of Zoology, Academia Sinica; Guo Lihe [6753 4409 0735], Shanghai Institute of Cell Biology, Academia Sinica; et al.]

[Abstract] The ovine genomic library containing 9.7 x 10^6 pfu recombinants was constructed by using bacteriophage $EMBL_3$ as vector and testis DNA of Xinjiang fine wool sheep as insert. Firstly the library was screened using a fragment of hormone (GH) gene and six positive clones were obtained. Secondly the above six clones were screened using a synthesized 22mer corresponding to the sequence in a conserved region at the 5'-120 bp of the GH gene and three positive clones which contain the complete GH gene were picked out. One clone of three intact GH clones was mapped. The result showed that the ovine GH gene was located in the middle of the inserted fragment.

The Synthetic Oligodeoxynucleotides Activate PHO5-lacZ Fusion Gene Expression

40091004B Shanghai SHENGWUHUAXUE YU SHENGWUWULI XUEBAO [ACTA BIOCHIMICA et BIOPHYSICA SINICA] in Chinese Vol 22 No 5, Sep 90 p 433

[Article by Zhu Shengzu [2612 4939 4371], and Yu Qin [2456 0530], et al.; [Shanghai Institute of Biochemistry, Academia Sinica]

[Abstract] In accordance with the structure of upstream activation sequences of PHO5 and PHO11 genes, a series of oligodeoxynucleotides has been synthesized and tested for control of the PHO5-lacZ fusion gene expression. A 30-bp UAS mutant conferred high level regulated gene expression with respect to the concentration of

phosphate. The dyad symmetric 18-bp sequence within the mutant may be very efficient for binding to the regulatory factor. The synthetic segments can be used to study the interaction between protein and DNA and to construct the vectors for high level expression of heterologous genes.

Structural Analysis of Oligosaccharides from Ricinus communis Agglutinin

40091004A Shanghai SHENGWUHUAXUE YU SHENGWUWULI XUEBAO [ACTA BIOCHIMICA et BIOPHYSICA SINICA] in Chinese No 5, Sep 90 p 425

[Article by Gu Xin [7357 2450], Sun Ce [1327 0374] and Shen Zhaowen [3088 2507 2429], Shanghai Institute of Biochemistry, Academia Sinica]

[Abstract] To release the sugars from Ricinus communis agglutinin (RCA_I, hydrazinolysis was applied. After the oligosaccharides were reduced with $NaBH_4$, they were passed through a Bio-gel P-4 column and three major oligosaccharides were obtained. The purified oligosaccharides were permethylated, hydrolysed and acetylated, and PMAA (partially methylated alditol acetate) was collected. GC-MS was used to determine the linkage between sugars. Some hydrazinolyzed oligosaccharides were reduced with NaB^3H_4, labelling them with ^3H. Glycosidases and Bio-gel P-4 gel filtration were also applied to determine the sequence and anomers of these oligosaccharides. The structure of oligosaccharide chains of RCA_O was postulated as follows:

Second Generation Artificial Blood Developed in Shanghai

91P60054A Shanghai WEN HUI BAO in Chinese 3 Nov 90 p 1

[Article by Jiang Shuzhi [5592 2885 5347]

[Summary] Having extensively studied the synthesizing process, the pharmacodynamics and pharmacokinetics of the fluorocarbon artificial blood, Wang Bingnan [3769 2671 2809] of Shanghai Institute of Organic Chemistry and Ding Xuncheng [0002 6064 6134] of Shanghai Institute of Industrial Hygiene and Occupational Diseases Control of the Chinese Academy of Sciences (CAS) have developed a second generation artificial blood. In 1986, the Shanghai Science Commission ordered the study of a second generation artificial blood to solve such problems as short preservation time, short half-life, and incompatibilities encountered in using first generation artificial blood developed by the Third Military Medical College and the Shanghai Institute of Organic Chemistry in the early 1980s. The newly developed blood has extended the blood's preservation time and half-life from 6 months to 18 months and from 10 hours to 19.8 hours respectively. The particles, about one-seventieth the size of normal human erythrocytes, enable the oxygen-rich artificial blood to go around the clots and release oxygen to oxygen-deficient areas. The newly developed artificial blood can also be used to replace all types of human blood without causing cross reactions, and it will protect patients from being infected with transmitted diseases because of its advantage of sterilizability in the manufacturing process. The advantage of being able to mix with other types of blood will maintain normal blood and visceral functions of patients who have been seriously injured. Studies on artificial blood's ability to carry oxygen, its coagulation information and problems encountered in immunization process are under way. Recently, the Shanghai Science Commission decided to allocate funds for intermediate tests of the second generation blood before moving into large-scale production.

Immobilized-Living-Cell Fermentation Technique Developed

91P60054B Beijing BEIJING KEJI BAO in Chinese 24 Nov 90 p 1

[Article by Wang Kexiang [3769 0344 4382] and Sui Rui [5685 3843]; Breakthrough in Vinegar Fermentation Technique Using Immobilized Living Cells]

[Summary] A new technique for vinegar fermentation has been developed by Beijing Foodstuff Brewing Institute of the Ministry of Commerce. After 2 years' extensive study, the institute obtained two kinds of high-quality, immobilized living cells: 211 and 212 (carrier). The fixed living cells are the complete enzyme systems containing coenzymes, which can, under optimal conditions, undergo mass proliferation and complete a series of complex biochemical reactions. Tests conducted by the researchers have revealed that the two strains of fixed living cells could extend the normal cell's life span from 3000 hours to 4800 hours, cut total time for fermentation cycle down to less than 15 days, raise total acidity of vinegar product to equal to or greater than 40 and the reducing sugar content to more than 1 percent. The new technique for fixing acetobacters and yeasts for vinegar fermentation can be used to fix other microorganisms as well. It can also be expanded to all fermentation industries in order to achieve high-quality, high-output production by using smaller, more efficient facilities. The adoption of this new technique in the fermentation plants will eventually reduce pollution problems created by brewery industries.

Advances in Fermentation Engineering

91P60054C Beijing KEJI RIBAO [SCIENCE AND TECHNOLOGY DAILY] in Chinese 5 Nov 90 p 2

[Article by Li Xigen [2621 3588 2704]; East China College of Chemical Engineering Applies Biosensor in Fermentation Engineering]

[Summary] A new biosensor, a heat-sensitive penicillinase electrode, was developed by the Institute of Biochemical Engineering and Institute of Applied Chemistry of East China College of Chemical Engineering for

fermentation engineering. The newly developed biosensor has shown such superior features as fastness, stability and having a long life. Another achievement of the institute is the application of computers in controlling penicillin fermentation. Because of the adoption of these new techniques, the Shanghai Third Pharmaceutical Plant has developed new penicillin-producing bacterial strains, elevated the fermentation units to 16.7 percent, and increased profits to 1.8 million yuan. The institute is extending the applications of these achievements to other antibiotics-producing plants.

Snake Venom Research Organizations

91P60072 Nanning SHEZHI [JOURNAL OF SNAKE] in Chinese Vol 2, No 3, 15 Sep 90 p 1

[Article by the Editorial Department of the JOURNAL OF SNAKES]

[Summary] The organs responsible for snake venom research and pharmaceutical production are the three snake research organizations—the Chinese Snake Association's Snake Venom Research Institute, the Snake Venom Clinical Study and Application Center of the People's Liberation Army, and the Qingfeng [7230 1496] Pharmaceutical Plant in Fushun—all located in the No. 238 Hospital of the Fushun Military District in Liaoning Province. These three official organizations bring together snake venom research and product manufacturing, which systematically combine snake breeding, venom extraction and research, pharmaceutical production, and clinical application in one location. The major pharmaceutical product of the organizations, Qingshuanmei (embolus-dissolving enzyme) developed by Professor Qin Gongping [6009 0361 1627] of the No. 238 Hospital of the People's Liberation Army, is one of their enzyme preparations from snake venom and has been succdssfully applied in treating cardiac and cerebral ischemic diseases. Another snake venom preparation, "Qinglong Changrong Capsule", recently developed by the Snake Association's Snake Venom Research Institute, is said to be more effective and bring fewer side effects to patients.

Neural Network Expert Systems and Their Application in Nuclear Reactor Fault Diagnosis

40101122 Beijing DIANZI XUEBAO [ACTA ELECTRONICA SINICA] in Chinese Vol 18 No 6, Nov 90 (MS received Oct 88, revised Mar 90) pp 62-68

[Text of English abstract of article by Yang Yiping and Tai Juwei, Institute of Automation, CAS]

[Text] Abstract: The neural network is a new kind of representational model which differs from the current logical model. In the paper, we apply it to RODES—an expert system for diagnosing nuclear reactor faults and propose the idea of neural net heuristics. The parallelism, distribution and learning capabilities of neural net heuristics provide a new way for knowledge acquisition, knowledge representation and fuzzy inference in expert systems. Actual practice in nuclear reactor fault diagnosis shows the system's potential power in research on artificial intelligence.

Development of New Robots Described

Underwater Robots Made by CAS

91FE0152A Beijing BEIJING KEJI BAO [BEIJING SCIENCE AND TECHNOLOGY NEWS] in Chinese 24 Oct 90 p 1

[Article by Zhou Wenlei [0719 2429 4320]: "Underwater Robot Made by CAS Enters Worldwide Marketplace"]

[Text] A robot is a combination of conventional machines and electronic technology. The use of robots has significantly improved productivity and promoted automation in various industries. In the early 1980's, high-tech competition in robotics began. Japan has successfully developed and used robots and has attracted attention from all over the world. Under the concern of Premier Zhou, we began to closely follow robot development in Japan since 1972. Studies on "new technology revolution and its countermeasures" began in the early 1980's. During the planning stage of the Seventh 5-Year Plan, CAS proposed establishment of an open robot research and development base—the "robot demonstration project"; it was officially listed as a national Seventh 5-Year Plan project. This project was put into operation in January 1989, and involves a government investment of a total of 58.774 million yuan and $5.9 million of foreign exchange. The facility occupies over 70,000 square meters of land with 34,000 square meters of building space. On the basis of pre-inspection, the "robot demonstration project" was accepted by the government on 31 August 1990. The national inspection and acceptance committee included experts from the State Planning Commission, State Science Commission, construction industry, Ministry of Machine-Building and Electronic Industry, Ministry of Aerospace Industry, Ministry of Economics and Trade, province of Liaoning, city of Shenyang, Shanghai Jiaotong University and Qinghua University. The committee believes that scientific management at the robot demonstration project would result in accelerated progress, high quality and significant benefits. A notice from CAS was announced at the acceptance meeting. The official name of the robot demonstration project is "CAS Shenyang Robotics Engineering R&D Center."

This is an important project in the development of high technology and implementation of the 863 Plan. Its completion and use marks a new plateau in the development of intelligent robots in China, and it will play an important role in accelerating progress in this area. From now on, China has a base to produce robots and to develop and manufacture more products.

A medium-size underwater robot, Recon-IV-300-SIA-02, developed by CAS Shenyang Institute of Automation, is being sold to the United States.

Recon-IV, a medium-size underwater robot, was a key technical hurdle to overcome in the Seventh 5-Year Plan. During the development process, in order to start from a more advanced point and to accelerate its progress, on the basis of its prototype "Hairen 1," Shenyang Institute of Automation successfully utilized technology brought over from the United States. After more than 3 years of hard work, the institute not only digested and absorbed imported technology but also made some innovations. This made it possible to develop this world-class high-tech product in the Seventh 5-Year Plan.

Ninety percent of the parts going into Recon-IV are manufactured in China. CAS takes full advantage of its matching technology to improve the imported technology. The original product was for observation only and it can operate with several functions now. The robot is equipped with audio, video and sonar units and has two hands capable of performing five or six functions. This innovation is not found on similar underwater robots made abroad. In addition to closed-loop control of depth, closed-loop control of direction of navigation has been added. The propelling power of the system also has been increased 1.8 times. Its payload has also been increased from 114 kg to 160 kg. Its speed has been raised from 2.5 to 3 knots. It can operate in a high-ocean current. This makes it the leader among similar products in the world. Perry Company in the United States praised this medium-size underwater robot and decided not to produce this class of underwater robots in the United States. Therefore, China is the first choice for anyone who needs it.

In addition to importing medium-size underwater robot technology, CAS also addresses the development of domestic and international markets. It provides services such as demonstration to users, renting and leasing, and after-sale service.

In October 1987, during the demonstration at Fengman Power Plant, it provided front-end services for the expansion project at the plant. Valuable video data was obtained which served as a decisive basis for the expansion project. The plant then decided to purchase a light-weight-model underwater robot, the "Gold Fish." It was the first underwater robot used in a hydroelectric dam in China.

From December 1988 to August 1990, this underwater robot was successfully used six times in servicing offshore oil-drilling rigs in the South China Sea and at the mouth of the Zhujiang River. With excellent maintenance skill and sufficient spare parts and accessories, the technical staff earned high praise. For the first time, a Chinese-made underwater robot was used in offshore oil drilling in China. At the present moment, in addition to oil drilling, it is also used in sea rescue missions and dam inspection and repair.

Shenyang Institute of Automation has the capability to manufacture heavy, medium and light underwater robots. Furthermore, it can provide a standard underwater robot according to customer requirements within 24 weeks. This speed is comparable to that for similar products abroad.

Intelligent Robot Debuts in Tianjin

91FE0152B Shanghai WEN HUI BAO in Chinese 1 Nov 90 p 1

[Article by Xu Qianwei [6079 0467 0251] and Liu Youlin [0491 0645 2651]: "Robot Debuts in Tianjin"]

[Text] For the first time, China has a robot with an intelligent hand. It can see and hear, and has the sensation of touch. It is capable of carrying out hazardous and toxic operations with outstanding performance. Its capability was fully demonstrated in today's certification process. Experts believe that this research effort accomplished in Tianjin is of world-class level as of the 1980's. It is at the cutting edge in China.

This intelligent robot system is a key project undertaken in Tianjin. It was a joint effort between Nankai University and Tianjin University for 3 years. The NKRC-03 robot-control system was developed by the Department of Computer and Systems Science at Nankai University. It uses the most advanced NKV robot language and employs a variety of sensors for information control. Therefore, it has high-level-language programming capability to form a continuous sensing system for force and vision. This is a standard second-generation robot. The intelligent hand was developed by Tianjin University. It can be pneumatically or electrically operated and has the sensation of touch. It can automatically control the amount of force when it grabs an object.

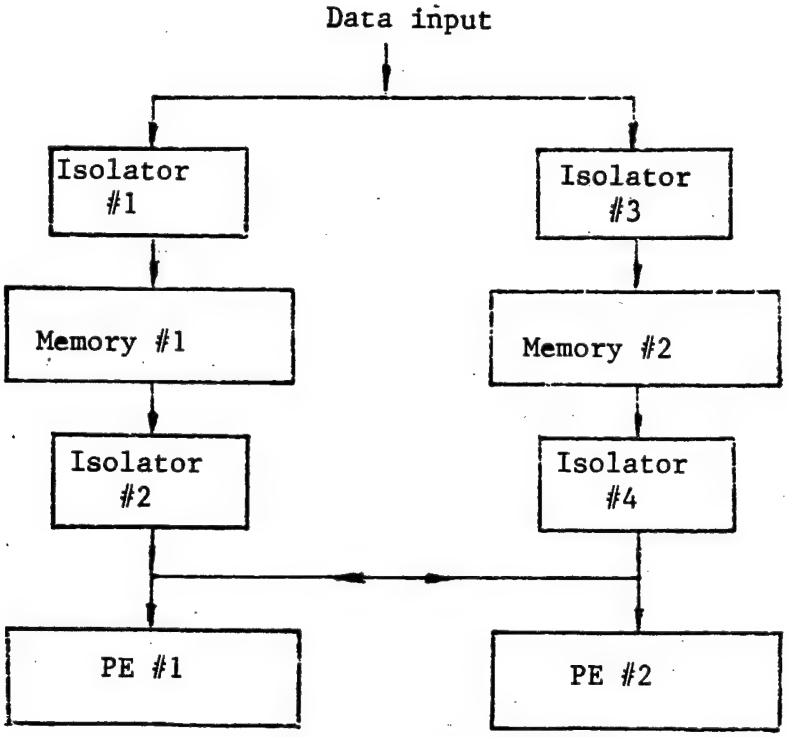

Figure 2. Schematic Diagram of Ping-Pong Memory (PE denotes processing element)

Application of TMS320 Parallel Processing Technology for Ground Surveillance Radar Signal Processing

91P60056A Chengdu DIANXUN JISHU [TELECOMMUNICATIONS ENGINEERING] in Chinese Vol 30 No 3, Jun 90 pp 6-11 (MS received 5 Mar 90)

[Article by Jian Ming [4675 2494], Graduate Student at Research Institute 10 of the Ministry of Machine-Building & Electronics Industry, and Dai Qingfen [2071 1987 5358], Research Fellow at same institute]

[Summary] In this research paper, the application of two Texas Instruments TMS320C25 digital signal processing chips to the design of a real-time parallel signal processing circuit for a pulse doppler ground surveillance (moving target) radar is described.

Selected characteristics of the TMS320C25 chip follow: 100-nanosecond instruction cycle, 32-bit accumulator, 16-bit data bus, 16-bit address bus, 100 nanoseconds required for a 16 x 16-bit multiplication, 544-word built-in RAM, 64Kword directly addressable external data memory space, 64Kword external program storage space, and 16 I/O channels.

Two key problems in the design of a parallel-processing system are covered: the "bottleneck" effect in data input and the synchronous coordination of the two chips. In overcoming the first problem, the authors use a "ping-pong" memory, as shown in Figure 2 [Fig. 1 not reproduced].

Memory devices 1 and 2 are each 32K capacity; note that both memories can be used by each PE (TMS320C25). Operation is as follows: when memory 1 is being loaded with the data input (output from radar antenna), isolators 1 and 4 are gated [i.e., switched on], isolators 2 and 3 are switched off, and PEs 1 and 2 can access data stored in memory 2. For the next data frame, during which memory 2 is being loaded with the external data, memory 1 provides data to the PEs, isolators 2 and 3 are gated, and isolators 1 and 4 are switched off. The address generation circuit for the PEs uses four 74HC161 chips to form a 16-stage counter.

In overcoming the second problem, the basic goal is to design a circuit eliminating access conflicts. This problem is often solved with hardware, but that approach requires more space and thus goes against one of the design objectives: a more compact system. The authors therefore chose a software approach, revolving around software instructions to the two general-purpose I/O pins of the TMS320C25, the BIO bar and XF pins. The two PEs are connected together as shown in Figure 3.

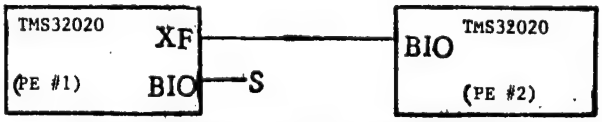

Figure 3. Synchronous Coordination Circuit (S denotesselect line)

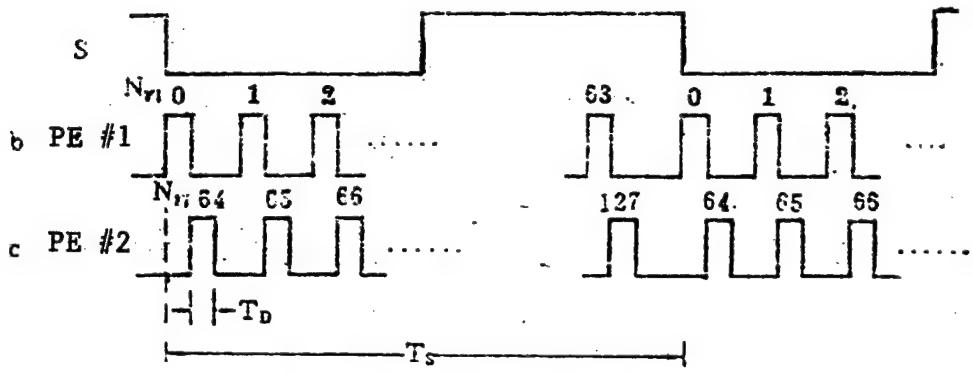

Figure 4. Synchronization Coordination Sequence

The pulses for the synchronous coordination sequence are shown in Figure 4.

Note that for the experimental system, Texas Instruments TMS32020 chips were used instead of the TMS320C25 chips.

Results are as follows: FIR [finite impulse response] and FFT [fast Fourier transform] signal-to-noise improvement factors in the software simulation (TMS32020 simulation software) were 13.68 and 16.77, respectively; and 13.24 and 15.47, respectively, in the analog system (i.e., as measured with an analog source). Theoretical values are 13.57 and 16.57, respectively. Measured suppression ratio for the FIR filter with respect to a fixed target was 43.68dB, and 41.06db for the FFT with respect to a fixed target. The entire system's processing speed is 20 million multiplication/addition operations per second, volume is 14 x 40cm^2, and power consumption is 5 watts.

References: 5 English, 3 Chinese.

Electrostatic Free-Electron-Laser Wiggler

91FE0117A Beijing DIANZI KEXUE XUEKAN [JOURNAL OF ELECTRONICS] in Chinese Vol 12 No 5, Sep 90 pp 552-556 [MS received 12 Dec 88, revised 20 May 89]

[Article by Wang Qingyuan [3769 3237 3293] of the University of Electronic Science and Technology, Chengdu: "Electrostatic Free-Electron-Laser Wiggler"]

[Excerpts] Abstract

An electrostatic free electron laser (FEL) can use an electrostatic wiggler, instead of a magnetostatic wiggler, to generate coherent radiation. This paper presents an electrostatic FEL wiggler which is capable of generating a circularly polarized wiggler field of a relatively large amplitude at a period of 3 cm to 5 mm. This wiggler will facilitate further research in FELs.

1. Introduction

There have been a number of studies done on FELs.[1-6] An electrostatic FEL using either a periodic transverse or longitudinal electrostatic field has also been investigated.[7-9] The wiggler field of the electrostatic wiggler introduced in this paper is generated by the potential difference between conductors; therefore, it can overcome the current-induced thermal effect of a double spiral magnetostatic wiggler. This electrostatic wiggler has a simple structure and is capable of providing a large-amplitude wiggler field at a period ranging from 3 cm to 5 mm.

2. Electrostatic Wiggler and Electrostatic Wiggler Field

Figure 1 is a schematic diagram of an electrostatic wiggler of infinite length. It consists of a hollow dielectric cylinder and a pair of spirally wound conductors embedded in it. The inner and outer surface of the hollow dielectric cylinder and the cylindrical plane at the center of the spiral conductors divided the entire space into parts I, II, III and IV. The inner and outer diameters of the dielectric cylinder are R_1 and R_2, respectively; the radius of the cylindrical plane at the center of the spiral is b, the period of the spiral is L, and the radius of the spiral is δ. The dielectric constants of the media are ε and ε_o, respectively. The electric potential is $+V_0/2$ on one conductor and $-V_0/2$ on the other. [passage omitted]

3. Amplitude of Electrostatic Wiggler Field

The electrostatic wiggler field is generated by a pair of spiral conductors with a fixed potential difference. Its field strength cannot exceed the vacuum spark discharge level E_b in zone I and it cannot be higher than the dielectric strength E_{bd} in the dielectric. Otherwise, the wiggler might be damaged due to spark discharge or dielectric breakdown. In the electrostatic wiggler shown in Figure 1, if the dielectric strength E_{bd} is very high, the field strength in zone I will exceed E_b when V_o increases.

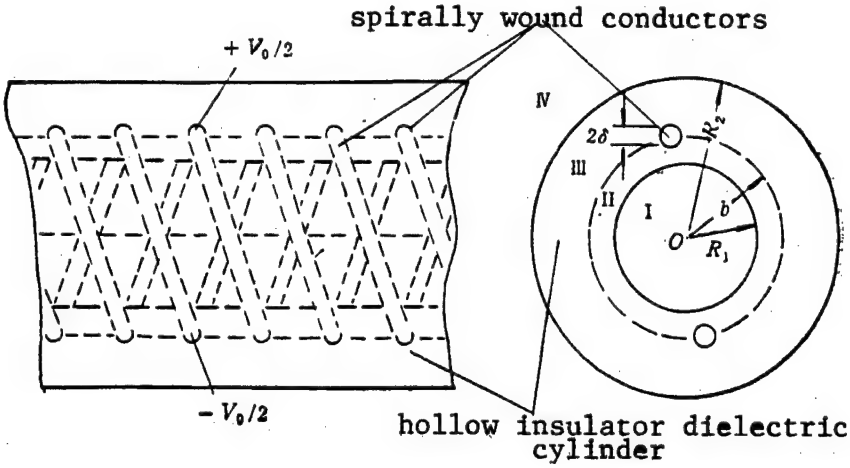

Figure 1. Schematic Diagram of the Electrostatic Wiggler

The maximum field strength in zone I is at $r = R_1$, $\varphi - kz = \pi/2 + 2l\pi$. In order to ensure safety, the field strength there must be less than E_b:

$$\left|E_{\mathrm{I}}\right|_{\substack{r=R_1 \\ \varphi - kz = l2\pi + \pi/2}} \left| \sum_{n=1}^{\infty} A_n nk I'_n (nkR_1) \sin(n\pi/2) \right| < E_b \qquad (28)$$

From equations (28) and (26), together with (19)-(25), it is possible to obtain the voltage limit applied to the two conductors. In the dielectric, the maximum electric field occurs at $r = b - \delta$, $\varphi - kz = 2l\pi + \pi/2$. It is

$$\left|E_{\mathrm{II}}\right|_{\substack{r=b-\delta \\ \varphi - kz = l2\pi + \pi/2}} \left| \sum_{n=1}^{\infty} B_n nk I'_n[nk(b-\delta)] \sin(n\pi/2) + \sum_{n=1}^{\infty} B'_n nk K'_n[nk(b-\delta)] \sin(n\pi/2) \right| \qquad (29)$$

Many dielectric materials, such as quartz, polytetrafluoroethylene, polystyrene and boron nitride, have very high dielectric strength. Many have been used in experimental studies on the Cerenkov FEL.[10,11] Table 1 shows the maximum amplitude at the center axis of the wiggler field and the corresponding maximum dielectric field strength with polystyrene. The dielectric constant for polystyrene is 2.53[12] and its dielectric strength is 6 x 10^8 V/m.[13] The breakdown field strength in vacuum is 4 x 10^7 V/m.[13]

From Table 1, at a period of 3 cm, an electrostatic wiggler without a dielectric cylinder can generate an amplitude of 1.1 x 10^6 V/m. With a dielectric cylinder, it is raised to 2.5 x 10^7 V/m. Therefore, it is obvious that a dielectric cylinder can effectively increase the amplitude of the wiggler field.

This type of electrostatic wiggler can produce a field of a shorter period. In Table 1, when L = 0.5 cm, the amplitude can still reach 1.5 x 10^7 V/m. With this kind of short-period wiggler field, it is possible to use a lower-energy electron beam to generate a coherent radiation at a higher frequency. This would be very valuable in practical applications of the FEL.

Table 1. Maximum Amplitude of Electrostatic Wiggler Field

Wiggler Period L (cm)	Inner Radius of Dielectric Cylinder R_1 (cm)	Spiral Radius b (cm)	Outer Radius of Dielectric Cylinder R_2 (cm)	Wire Radius (mm)	Dielectric Constant	Maximum Amplitude of Wiggler Field E_0 (V/m)	Maximum dielectric Field Strength (V/m)
3	1.9	2	2.1	1	1	1.1 x 10^6	—
3	0.5	1	2	3	2.53	2.5 x 10^7	8 x 10^7
0.5	0.2	0.4	1	0.5	2.53	1.5 x 10^7	3.2 x 10^8

4. Conclusions

An electrostatic wiggler is presented in this paper. Analytical expressions of the wiggler field are obtained at infinite length, and the maximum amplitude is discussed. This wiggler has a simple structure; it overcomes the thermal effect caused by current and is capable of producing a circularly polarized field of substantial

amplitude near the axis. Furthermore, there is no current passing through the conductor which allows us to use thinner spiral wires to produce a short-period wiggler field. This wiggler itself is a dielectric waveguide. It is also possible to use a Gaussian light beam system. The transition of the wiggler field may be achieved by changing its radius at the end. The amplitude of the wiggler field can be further increased if a suitable dielectric material of higher dielectric strength is used.

The author wishes to express his gratitude to Professor Liu Shenggang [0491 4141 4854] for his direction and assistance and to He Yiping [0149 0001 1627] and Jiang Huabei [5592 5478 0554] for the beneficial discussion.

References

[1] Liu Shenggang, "Xiangduilun Dianzixue" ["Relativistic Electronics"], Science Publishing House, 1987.

[2] H. P. Freund, S. Johnston, P. Sprangle, IEEE J. OF QE., QE-19 (1983), 322.

[3] Y. Z. Yin, R. J. Ying, G. Bekefi, IEEE J. OF QE., QE-23 (1987), 1610.

[4] J. Fajans, G. Bekefi, PHYS. FLUIDS, 29 (1986), 3461.

[5] T. J. Orzechowski, W. W. Destler, IEEE J. OF QE., QE-21 (1985), 831.

[6] R. Chojnacki, W. W. Destler, IEEE J. OF QE., QE-23 (1987), 1605.

[7] A. Gover, P. Sprangle, IEEE J. OF QE., QE-17 (1981), 1196.

[8] A. Gover, APPL. PHYS., 23 (1980), 295.

[9] G. Bekefi, R. E. Shefer, J. APPL. PHYS., 50 (1979), 5158.

[10] H. Lashinsky, J. APPL. PHYS., 27 (1956), 631.

[11] S. V. Laven, et al., APPL. PHYS. LETT., 41 (1982), 408.

[12] L. J. Giacoletto, "Electronics Designers' Handbook," McGraw-Hill Book Company, New York, (1977), pp 2-46.

[13] S. Whitehead, "Dielectric Breakdown of Solids," Oxford University Press, (1951), p 75.

New Speed Sensor for Tanks, Missiles, Aircraft Developed

91FE0113E Beijing KEJI RIBAO [SCIENCE AND TECHNOLOGY DAILY] in Chinese 22 Oct 90 p 2

[Article by Li Jing [2621 4552]: "New Speed Sensor Developed"]

[Text] A research group led by Professor Zhang Fuxue [1728 4395 1331], a young expert who has already made significant contributions to his country, recently developed a new speed sensor—the "dynamic-start piezoelectric fluidic speed sensor." This sensor has important military applications, primarily in tank fire-control systems; it can also be used in automatic control systems for missiles, airplanes, ships and robots to measure rotational speed. Under the situation wherein this subject was kept as top secret in other countries, the group worked in collaboration with the technical staff at Beijing Science & Engineering University and at the state-run Huifeng [1920 0023] Machinery Plant. After over 2 years of investigation, the group completed successful development of this product. Trials conducted by the Ministry of Ordnance have demonstrated that the sensor meets specifications for the fire-control systems for three generations of main battle tanks. Compared to similar products made in the United States and Japan in 1980, it has 25 times higher sensitivity. Its threshold voltage has been optimized by one order of magnitude and dynamic activation has been realized. (Nothing of this kind has been reported abroad.)

Field-Emission Micro-Analysis System Developed

91FE0113B Beijing KEJI RIBAO [SCIENCE AND TECHNOLOGY DAILY] in Chinese 14 Oct 90 p 1

[Article by Liu Zhiwei [0491 1807 0251]: "Field-Emission Micro-Analysis System Developed"]

[Text] Abstract

A field-emission micro-analysis system was successfully developed by a research group led by Associate Fellow Liu Wu [0491 2976] of Central China Teachers' University and Associate Professor Ren Duomin [0117 1122 2404] of China Science and Technology University after nearly 3 years of hard work. At the certification meeting held at Central China Teachers' University, experts believed that it is the first of its kind in the world. This achievement provides a bright future for the revelation of micro-structures.

For a long time, field-ion-emission microscopy has been used to study atoms on a solid surface. A strong electric field is applied to the surface of the specimen in field-ion-emission microscopy. There are doubts about the experimental results. In order to solve this problem, the group led by Liu Wu and Ren Duomin had the idea to integrate an FEM (field electron microscope), an FIM (field ion microscope) and an IAP (imaging atomic probe) into one unit. Under the concern and support of the State Education Commission, the State Science Commission, and the National Natural Science Foundation, they overcame numerous problems in the 3-year development period to combine theory with practice, and have published close to 30 papers, many presented at conferences throughout the world.

In addition to having combined capabilities of an FEM, FIM and IAP, such as measuring work function, observing surface atomic arrangement and determining chemical composition, this field-emission micro-analysis

system has the abilities to analyze three-dimensional structure, study surface adsorption, depolarize and polarize, emit anions, and analyze the effect of field strength and lasers on material surface that other micro-analysis systems cannot perform. Furthermore, it can perform individual or comprehensive analysis of a sample on a real-time basis.

Warship-Borne Satellite Cloud Imagery Receiver Developed

91FE0113D Beijing KEJI RIBAO [SCIENCE AND TECHNOLOGY DAILY] in Chinese 18 Oct 90 p 1

[Article by Xu Wenhua [1776 2429 5478]: "Marine Satellite Cloud Imagery Receiver Developed"]

[Text] A satellite cloud imagery receiver system has been successfully developed by the Naval Weather Department and the 503rd Institute of the Ministry of Aerospace Industry. The system provides reliable scientific data for warships to safely and accurately avoid typhoons to prevent incidents.

This achievement was certified in Hangzhou on 11 October. Its technical performance is at a world-class level. It fills a void in the marine application of geosynchronous weather satellites.

Ultraharmonic Mixer Technology Applied to Laser Detection

91FE0113C Beijing KEJI RIBAO [SCIENCE AND TECHNOLOGY DAILY] in Chinese 16 Oct 90 p 2

[Article by Yue Ziqiang [2867 1311 1730]: "China's Ultraharmonic Mixer Technology Advances"]

[Text] For the first time, sub-millimeter-wave ultraharmonic mixer technology has been used in a difluoromethane far-infrared laser detection apparatus by CAS Shanghai Institute of Technical Physics (SITP) and the China Institute of Metrology (CIM). This achievement indicates that this project has reached a world-class level as of the late Eighties. This project, assigned by the State Economic Commission as a key project in the Seventh 5-Year Plan, was reviewed and certified by Professor Wang Daheng [3769 1129 3801], a famous expert in optics and a member of the committee of CAS.

Measurement of light frequency with high accuracy based on length and time is an important research subject in metrology. Measurement of far-infrared laser frequency is an important technical basis in light-frequency measurement and is a hot research subject. Only a few developed countries in the world are doing research in this area.

The GaAs Schottky-barrier-diode sub-millimeter-wave ultraharmonic mixer developed by SITP has a horn-shaped lens cross waveguide structure. It is a novel and unique far-infrared differential detector. A sub-system consisting of a sub-millimeter-wave harmonic mixer receiver using this device as its core component and the optically-pumped difluoro-methane laser developed by CIM using a short millimeter-wave solid-state oscillating source was used to detect the laser signal from the difluoro-methane laser at 1.397 THz (214 microns) after 15 and 19 times of harmonic mixing. Compared to similar work done abroad, the domestic research is at the ultraharmonic level. This latest achievement in far-infrared laser radiation detection provides us with an advanced technique and key components in light-frequency measurement. It not only has major scientific significance and obvious application value, but also lays a good foundation for developing the frequency spectra of sub-millimeter waves.

Optical-Waveguide-Fiber Industrial Endoscope

91FE0113A Beijing KEJI RIBAO [SCIENCE AND TECHNOLOGY DAILY] in Chinese 6 Oct 90 p 2

[Article by Chen Yu [7115 3842]: "Optical-Waveguide-Fiber Industrial Endoscope"]

[Text] A high-tech high-accuracy non-destructive optical-waveguide-fiber industrial endoscope, Model GKT-8, was successfully developed by Xuzhou Optical Instrument Corporation in Jiangsu. To date, the company has seven models of optical-fiber industrial endoscopes in 12 different specifications to form a complete product line that can totally replace imported products. It is estimated that 10 million dollars of hard currency can be saved yearly.

An industrial endoscope is a special instrument used to inspect hidden parts inside a curved pipe in any machinery. It can accurately pinpoint the damaged area without shutting down the machine or taking it apart. Furthermore, by means of photography and video monitoring, one can make certain measurements. This kind of instrument is widely used in industries such as electric power, petrochemicals, aviation, shipyards and metallurgy, railroads, weapons manufacturing and machinery building.

Techniques such as injection molding, net making and snake-joint making have been improved. The scope of the probe is expanded from 180° in two directions to 360° in four directions. In addition, the length of the tube is also extended from 1 meter to 8 meters. The probe diameter is reduced from 15 mm to 8 mm.

Key State Lab for Sound-Field Acoustic Information Technology Opened to Chinese, Foreign Researchers

91FE0145B Beijing KEJI RIBAO [SCIENCE AND TECHNOLOGY DAILY] in Chinese 4 Nov 90 p 2

[Article by Liu Qin [0419 0530]: "Key State Lab for Sound-Field Acoustic Information Technology"]

[Text] A key State Lab for Sound-Field Acoustic Technology is located in Zhongguancun, a famous science

park in China. It was built in 1987 on the basis of work done on propagation and interaction of sound sources and sound waves in different media and on sound reception and sensing at the Institute of Acoustics of the Chinese Academy of Sciences (CAS). It is open to both Chinese and foreign researchers.

Acoustics is a branch of physics. It is closely related to other disciplines in physics, and is also linked to other sciences, such as engineering science, materials science, earth science, life science, information science and energy science and technology. Therefore, it contains a wide range of contents and has a great deal of applications.

Modern acoustics was developed based on physics and other sciences such as electronics and information science. To some degree, the development of digital information processing since 1950 is related to a need in acoustics. However, rapid development in digital signal processing also has promoted the development of acoustics.

Currently, theoretical and applied studies of sound-field and acoustic information have become an important aspect of modern acoustics. They also signify modern acoustics. In the development of modern science and technology, applications of theories and techniques associated with acoustic information and its processing have become widespread. Acoustic sensing and identification have become an indispensable tool to explore nature. Processing of voice signals is an important aspect of artificial intelligence. The study of sound-field acoustic information technology is closely related to defense research, ocean development, environmental protection and ecology, establishment of life science, and development of the national economy. Many countries in the world have addressed this issue with sufficient support. For example, noted laboratories have been built in the United States, France, and Denmark to simulate hydroacoustics fields. The United Kingdom also has a well-known laboratory for air sound-field research.

The Institute of Acoustics of CAS is the most important place for conducting sound research in China. Some theoretical and experimental studies on sound-field physics have reached a world-class level. In the 1986 International Hydro-Acoustic Meeting in Canada, Chinese hydro-acoustic research was recognized as a leader in the world. In areas such as sound sensing and identification, sound signal processing technology, sound research in air, the institute has obtained a great deal of accomplishments and trained a large number of qualified people.

The major direction at the key State Lab for Sound-Field Acoustic Information Technology is the comprehensive processing of and experimental research on sound-field and acoustic information sources by combining theory and technology associated with sound physics, acoustic information and signal processing. The theory and method associated with sound sensing and identification is a combination of acoustic information, signal processing and sound-field physics. This is a key area of the lab.

Major areas of research of the lab include:

1. Sound-field theory and physics and computer simulation. Sound fields in various media, such as water, air and solids, are simulated. On the basis of theoretical research, characteristics of sound fields, laws governing sound propagation and interaction with the media are studied using experimental models. In addition, acoustic simulation of various objects in a sound field and theoretical and experimental studies of non-linear sound fields are also performed.

2. Theory and calculation of sound inversion. This includes acoustic fault inversion in inhomogeneous media such as ocean and atmosphere; acoustic inversion of objects in sound fields in air, liquids and solids; extraction of underwater layer structure and its acoustic parameters and underwater "acoustic visualization"; and inversion in biological and human subjects.

3. Detection and identification of sound sources and sound-making objects. This includes the extraction of reflected and diffracted acoustic parameters of objects in various media, as well as acoustic imaging, sound-source location in waveguides, and sound-source identification.

4. Natural sound-source information and its signal processing. This includes the detection of target signals and language signal processing.

5. Sound-field space-time treatment and sound signal-processing technology.

This key State Lab for Sound-Field Acoustic Information Technology is equipped with a number of eighties-level experimental instruments, including a VAX 8350 computer, microVAXII, Sun-3 work stations, array processors, 32-channel programmable filter Series 32, 14-channel data recorder Model SR51, plotter, ultrasound receiver/analyzer, high-performance image analyzer, multiple-waveform synthesizer, standard measurement amplifier, and 14-channel high-density data recorder.

Magneto-Optical Pulse Current Measurement Apparatus Developed

91FE0145A Beijing BEIJING KEJI BAO [BEIJING SCIENCE AND TECHNOLOGY NEWS] in Chinese 27 Oct 90 p 1

[Article by Xin Wen [6580 2429]: "Magneto-Optical Pulse Current Measurement Apparatus Developed, Reaches World-Class Level"]

[Text] A group led by Bai Xiuting [4101 4423 1656], professor of electrical engineering at Qinghua University, and supported by the National Natural Science Foundation has been studying the electro-optic measurement of transient high voltage. After over two years of effort, they have developed a magneto-optical pulse

current measurement apparatus which was certified by experts from the Department of Materials and Engineering of the National Natural Science Foundation.

Experts unanimously agree that major indicators of the magneto-optical pulse current measurement apparatus, such as current measurement range, rise time, frequency bandwidth, and signal-to-noise ratio, have met the world-class level set in the late 1980's.

The magneto-optical pulse current measurement apparatus is a passive sensor which measures high-voltage current pulses. It may be used in power systems, high-voltage laboratories, thunder current measurement, completely sealed modular electrical devices, high-efficiency pulse apparatus, plasma laboratories and electromagnetic pulse apparatus. It employs insulated optical fibers to transmit information across the high- and low-voltage ends, which simplifies the insulator structure. It has advantages such as fast response, excellent resistance against electromagnetic inference and ease of computer linkage. Countries such as the United States, the USSR, Japan, and the United Kingdom have invested a great deal of manpower and resources into this area for quite some time.

The group led by Professor Bai took full advantage of the latest technology developed abroad. Based on the actual situation in China, utilizing existing technical conditions available, they focused on applications. In their work, in addition to aiming at the advanced level in the world, they did a great deal of work on domestic production of components and price comparison. For example, the group tested over 10 domestically manufactured materials and selected an inexpensive magneto-optical crystal with excellent performance characteristics. Finally, all key components of the magneto-optical pulse current measurement apparatus developed are manufactured domestically.

FIR Laser Photoacoustic Detection System

91FE0151A Shanghai HONGWAI YANJIU [CHINESE JOURNAL OF INFRARED RESEARCH] in Chinese Vol 9 No 4, Aug 90 pp 321-324 [MS received 30 Aug 89]

[Article by Su Jinwen [5685 6930 2429] and Xiong Shouren [3574 1343 0088] of Laboratory for Infrared Physics, Shanghai Institute of Technical Physics, the Chinese Academy of Sciences, and Qian Menglu [6929 1125 7456/6922] and Wu Datong [0702 1129 0681] of Institute of Acoustics of Tongji University, project supported by the National Natural Science Foundation: "FIR Laser Photoacoustic Detection System"]

[Text] **Abstract**

A novel FIR (far infrared) laser photoacoustic detection system is reported. Preliminary results of sub-millimeter wave absorbance measurements for 18 amino acids and one powdered DNA sample using this system are given. The maximum root mean square (rms) deviation of the data is less than 4×10^{-4}.

Key words: FIR, sub-millimeter wave, laser, photoacoustic spectrum, photoacoustic detection.

I. Introduction

The absorption spectrum of a material is usually measured by transmission or reflection. However, it is very difficult to get any experimental results using conventional optical methods when the sample is very transparent, or very absorbant, or when the sample has complex reflective properties such as a powder or an amorphous solid. The newly developed photoacoustic spectroscopy (PAS) technique can effectively solve this problem. Furthermore, several visible and IR PAS detectors are available.[1] However, before the authors began this project, PAS detection in the far infrared (40 μm-3 mm) was still a blank.

FIR absorption is usually measured by Fourier transform spectroscopy (FTS).[2] However, it is very difficult to measure absorption in the far infrared if the sample is an opaque powder or if it has complex reflection properties. Especially biological samples, it is very difficult to get any result with FTS. Hence, biological samples are first dehydrated and then ground into powders. The powder is sparingly mixed into polyethylene powder which has good transmittance in the far infrared. This mixture is then pressed into a slice of specimen for optical measurement. Its transmission spectra are measured by FTS. The absorption of the biological sample is then derived.[3] In some cases, powders of a dehydrated biological sample are suspended in cyclohexane, which is transparent to FIR laser, to conduct the measurement.[4] Because biological specimens are destroyed, these methods cannot yield true experimental results.

We employed an optically-pumped far infrared laser as the radiation source and applied PAS technology to FIR. Sub-millimeter absorbance measurements were made for 18 amino acids and one DNA powder sample.

II. Measurement Principle and Experimental Apparatus

The principle of FIR PAS detection is essentially identical to that of laser PAS measurement.[1] The differences include the use of an optically-pumped FIR laser as its radiation source,[5] short sub-millimeter wave transmission and detection technology is used in the detection system, and results obtained by the authors over many years in photoacoustic cavity and photoacoustic detection are applied.[6-9]

Figure 1 shows the structure of the photoacoustic cell. The volume of the photoacoustic cavity is approximately 0.16 cm^3. The top of the cavity is a 1 mm thick, 12 mm diameter FIR window made of polyterafluoroethylene (PTFE). Below the cavity is a sample cell, approximately 0.08 cm^3 in volume. When a modulated focused FIR laser beam shines on the sample through the window, the sample is periodically heated due to absorption of FIR radiation. Furthermore, due to thermal conduction, the thin layer of air over the sample is also heated and begins to vibrate periodically to generate an acoustic vibration

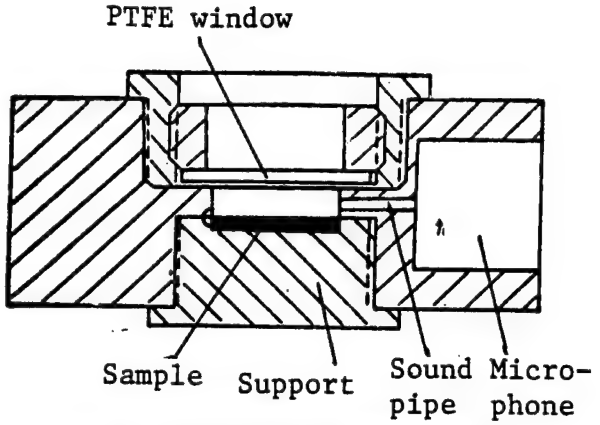

Figure 1. Structure of Photoacoustic Cell

inside the cavity. Its vibration frequency is identical to that of the laser modulating frequency f. The sound wave travels through a 1 mm diameter 6 mm long tube and is coupled to an electret capacitance microphone. It is then converted into electrical signals to be detected by a lock-in amplifier.

Figure 2 is a schematic diagram of the experimental FIR laser photoacoustic detection system. OPFIRL is the optically-pumped FIR laser system. It consists of a frequency-selecting $CWCO_2$ laser and a FIR waveguide laser and is capable of generating dozens of spectral lines ranging from several tens microns to a few millimeters.[10-11] In Figure 2, T is a gold-plated glass waveguide.[12] S is a sub-millimeter beam splitter made of Mylar film. C is a FM wave chopper. The modulated FIR laser beam is focused on the sample in the photoacoustic cell by lens F. P.C. stands for photoacoustic cell. The photoacoustic signal from the sample is V_s. Sample replacement is done under conditions that the photoacoustic cell remains constant to minimize system error. L_I and L_{II} are lock-in amplifiers. The reference signal of the tunable wave chopper C is simultaneously sent to L_I and L_{II}. D is a GAT-2P2 heat release detector developed by Shanghai Institute of Technical Physics. It has a flat frequency response over a wide range in IR and FIR.[13] The heat release detector D provides the baseline signal V_D for the FIR laser beam.

A 400 Hz chopping frequency was used in the experiment. The photoacoustic signal V_S and heat release detector signal V_D are input into a computer through lock-in amplifiers. The program automatically samples each specimen 100 times. The average is determined by the following equation:

This average based on (1) can eliminate the effect on the measurement due to fluctuation of the output power of

$$\overline{N}_S = 1/100 \sum_{1}^{100} V_S/V_D \qquad (1)$$

the FIR laser.

The soot produced by burning a mixture of alcohol and kerosene was used as the standard absorption specimen S_e. It is used to normalize the photoacoustic data for all specimens measured.

$$\overline{A}_S = \overline{N}_S/\overline{N}_{Se} \qquad (2)$$

All experimental data is processed, stored, and printed out by the computer.

III. Experimental Results

Table 1 lists the results of sub-millimeter absorbance measurement with 18 amino acids and one DNA powder. The computer also provides the mean square root deviation of each group. The data in Table 1 has a standard deviation of 1×10^{-5}-3.4×10^{-4}.

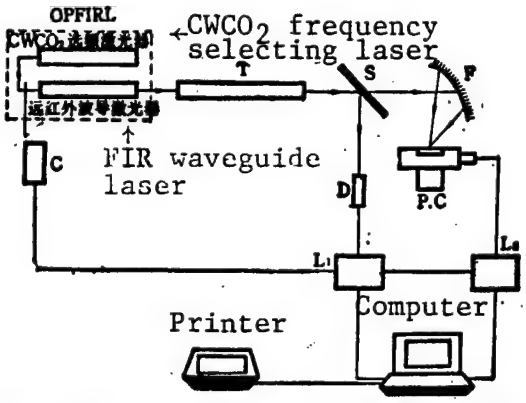

Figure 2. Schematic Diagram of the FIR Laser Photoacoustic Detection System

Table 1. Absorptivity of Amino Acid and DNA at Three Sub-Millimeter Lines

Number	Specimen	Absorptivity (percent)		
		118.8 μm	432.6 μm	447.2 μm
1	DL-a-alanine	7.5	13.0	14.5
2	Glycine	14.3	3.1	11.8
3	Asparagine	23.6	4.3	15.5
4	Glutamic acid	14.8	3.9	4.2
5	L-leucine	9.6	5.8	17.5

6	Valine	7.3	3.1	7.2
7	DL-serine	9.2	2.0	3.9
8	L-lysine	7.8	2.7	3.5
9	L-tyrosine	4.2	1.7	5.1
10	L-histidine	10.2	1.7	8.9
11	L-arginine	11.9	2.5	7.2
12	L-tryptophan	3.6	2.7	13.4
13	L-threonine	3.8	1.6	3.6
14	D-phenylalanine	5.9	1.2	6.3
15	L-methionine	3.2	2.5	6.5
16	L-cysteine	7.2	1.7	5.7
17	L-aspartic acid	4.4	1.4	3.9
18	DL-isoleucine	2.9	1.2	6.0
19	DNA	6.5	4.4	14.5

IV. Conclusions

(1) We have successfully established a FIR laser photoacoustic detection system and used it to measure 18 amino acids and one DNA powder. The maximum standard deviation is 4×10^{-4}.

(2) The normalization condition (soot) for absorption needs additional research and further improvement. This is because the FIR absorption spectrum of this soot has not been measured due to lack of resources.

(3) In this study, only three sub-millimeter lines were used. In order to obtain FIR photoacoustic spectra, work on other lines is in progress.

Acknowledgment: The authors wish to thank Hu Nengshu [5170 5174 2579] and Zhu Zerui [2612 3419 3843] of the Institute of Biology, Hunan Normal University for the specimens and for their collaboration.

References

1. Yoh-Han pao, Optoacoustic Spectroscopy and Detection, New York, Academic press, 1977, 194-238.

2. Shen Xuechu [3088 1331 4342], WULIXUE JINZHAN [PROGRESS IN PHYSICS], 2 (1982), 3, 275-322.

3. Husain, S. K. and Hasted, B., 7th Inter. Conf. on IR & mm Waves, Conf. Digest, 1982, p 24.

4. Tadashi, Fuse, et al., 9th Inter. Conf. on IR & mm Waves, Conf. Digest, 1984, pp 27-28.

5. Mary, S., Tobin Proc. IEEE, 73 (1981), 1: 61-85.

6. Qian Menglu, GUANGXUE YU GUANGPU JISHU [OPTICAL AND SPECTROSCOPIC TECHNOLOGY], (1982), 4: 142-5.

7. Qian Menglu, Wei Mohe [7614 1075 4139], SHENGXUE XUEBAO [JOURNAL OF ACOUSTICS], (1983), 6: 321-330.

8. Wei Mo-an, Qian Melu, 14 11th IcA, Paris, (1963), 8: 299-302.

9. Qian Menglu and Wei Mohe, SHENGXUE JISHU [ACOUSTIC TECHNOLOGY], (1985), 12: 1-6.

10. Su Jinwen, et al., HONGWAI YANJIU [CHINESE JOURNAL OF INFRARED RESEARCH], 3 (1984), 1: 26-32.

11. Su Jinwen, et al., HONGWAI YANJIU [CHINESE JOURNAL OF INFRARED RESEARCH], 5 (1986), 3: 167-174.

12. Xiong Shouren, et al., HONGWAI YANJIU [CHINESE JOURNAL OF INFRARED RESEARCH], 5 (1986), 3: 161-166.

13. Chen Zupei [7115 4371 1014] and Gu Junxia [7357 0689 0204], HONGWAI YANJIU [CHINESE JOURNAL OF INFRARED RESEARCH], 5 (1986), 5: 384.

GaAs/GaAlAs Quantum Confined Stark Effect, Self Electro-Optic Bistable Effect

91FE0050A Beijing BANDAOTI XUEBAO [CHINESE JOURNAL OF SEMICONDUCTORS] in Chinese Vol 11 No 9, Sep 90 pp 659-663 [MS received 26 Sep 89]

[Article by Wu Ronghan [0702 2837 3352], Duan Hailong [3008 3189 7893], Zeng Yiping [2582 0001 1627], Wang Qiming [3769 0796 2494], Lin Shiming [2651 0013 7686], Kong Meiying [1313 2734 1758], Zhang Quansheng [1728 2938 3932], Jiang Desheng [3068 1795 3932], and Xie Maohai [6200 5399 3189] of CAS Institute of Semiconductors, supported by the Chinese National Natural Science Foundation: "Experimental Investigation on GaAs/GaAlAs Quantum Confined Stark Effect and Self Electro-Optic Bistable Effect"]

[Text] **Abstract**

A GaAs/GaAlAs self electro-optic effect device (SEED) with a MQW (multiple quantum well) pin [positive-intrinsic-negative] structure has been fabricated. Its photocurrent spectrum and photocurrent-voltage characteristics have been analyzed. Problems associated with the realization of its optical bistability are also discussed.

Key words: optical bistability, MQW device, self electro-optic effect.

I. Introduction

Quantum confined Stark effect (QCSE) involves changes in quantized energy levels and transition probabilities in a superlattice quantum well (including two-dimensional free exciton) under an applied external electric field. The study of this effect not only has profound physical significance, but also may present a wide range of future applications for semiconductor electro-optic devices (for purposes such as optical bistability, optical switching, optical phase and amplitude modulation, laser wavelength modulation, etc.). Presently, due to the need in optical communications and optical data processing, studies on the QCSE associated with superlattice quantum-well GaAs/GaAlAs and GaInAsP/InP are very active and major progress has been made.[1-3]

The self electro-optic effect utilizes the QCSE and a suitable design of devices (or components) to enhance this electric field effect by light to obtain a positive feedback. When this positive feedback reaches a certain intensity relative to the input light signal, the output signal (transmitted light, reflected light, etc.) becomes a switchable and bistable output. With the switching and bistable effect, the device is a hybrid unit acting as a light receiver and a modulator. It has a variety of flexible combinations, consumes very little energy and operates very fast. Hence, it has a bright future.[4]

This paper primarily discusses problems associated with using photocurrent spectrum to study the QCSE and the bistability and switching effects due to self electro-optic effect and provides some experimental results.

II. Specimens and Experimental Conditions

The photocurrent spectrum measurement apparatus is shown in Figure 1. The specimen used is the GaAs/GaAlAs MQW pin structure prepared at the institute. Layer i of the MQW was not doped. Its conductivity is determined by the residual impurity. Figure 2 shows a schematic diagram of the structure of the device. The well is typically 80-120 Angstroms, the barrier width is typically 60-100 Angstroms, and the number of wells is usually 40-60. The aluminum content is usually 0.2-0.4. Therefore, the total thickness of the quantum wells is under 0.6 μm (not including barrier width). At 7500-8700 Angstroms, the optical absorption length is $\geq$ 1 μm. For a given incident light, light absorption and the excited carriers are considered to be uniform in the quantum wells. Layer i grown in a domestically manufactured MBE (molecular beam epitaxy) system was used. Its residual impurity concentration is in the range of 10^{15} cm^{-3} and its space charge width is in the submicron-to-micron range. The main source of photocurrent comes from excited carriers in the space charge region. Under this situation, a reverse bias photocurrent spectrum can directly reflect the absorption process and electric field effect in the MQW junction. In the samples used, under the condition that GaAs quantum wells are uniformly excited within a short wavelength range far away from the exciton absorption peak, carriers are always confined in the quantum well region. Neglecting the diffusion current, a simple analysis shows that the relation between the photocurrent J and reverse bias V is as shown in Table 1.

Table 1

Electric field/Space charge region	Weak field $v << v_{th}$	Strong field $v \leq v_{th}$
$d < W$	J proportional to V	J proportional to $V^{1/2}$
$d \geq W$	J proportional to $V^{1/2}$	J independent of V

In the table, v is the carrier drift velocity in the space charge layer in region i, v_{th} is the carrier thermal velocity, d is the width of the space charge region, and W is the total thickness of quantum wells and barrier. It is possible to study the expansion of the space charge region in the quantum wells based on the J-V curves. Figure 3 shows the J-V curves from three different sample chips. Within the applied voltage range, the space charge region d for sample 1 increases with voltage. However, $d < W$ (lower than breakdown voltage) is satisfied. Therefore, J is proportional to V. In sample 2, the space charge region has extended out of the quantum well region and J is independent of V. Sample 3 is somewhere between 1 and 2. With increasing bias, a transition from $d < W$ to $d \geq W$ takes place. Therefore, the variation of J as a function of V can provide useful information on the i region structure and the electric field distribution in a device.

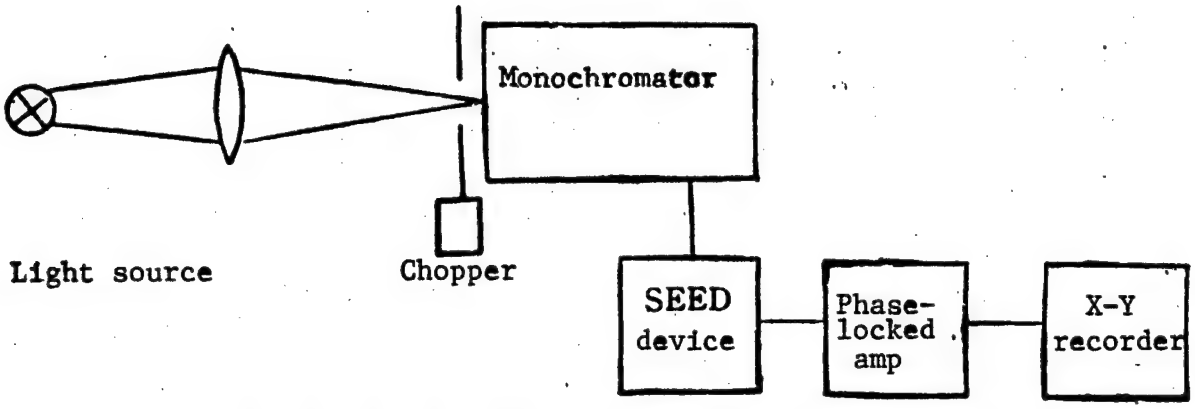

Figure 1. Room Temperature Photocurrent Spectrum Measurement Apparatus

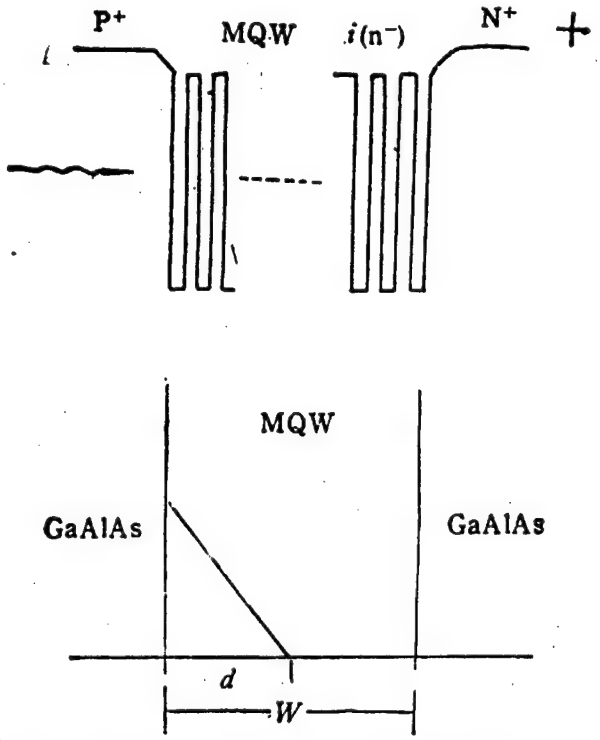

Figure 2. Schematic Diagram of Device Structure

III. Electric Field Effect of Optical Transitions Associated With Quantum-Well Energy Levels

Figure 4 shows typical photocurrent spectra under different reverse-bias levels in the light- and heavy-hole exciton absorption region.

1. With regard to the HH1-CB1 transition with $n = 1$, $\Delta n = 0$, it shifts toward longer wavelength with increasing electric field. Furthermore, the transition intensity drops.

2. With regard to the HH2-CB2 transition with $n = 2$, $\Delta n = 0$, it shifts toward shorter wavelength with increasing electric field. Furthermore, the transition intensity drops.

3. With regard to the HH2-CB1 transition with $n = 1$, $\Delta n = -1$, it shifts toward longer wavelength with increasing electric field. However, the transition intensity goes up significantly.

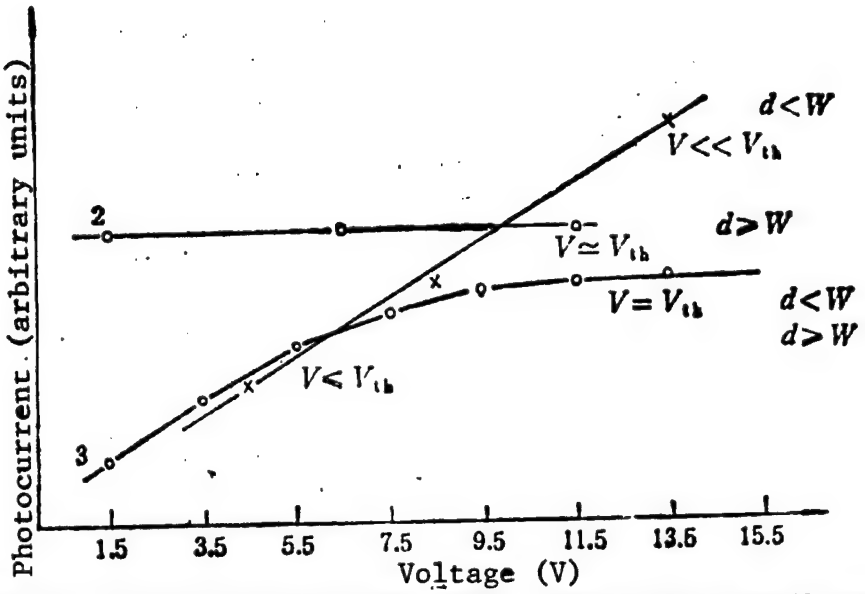

Figure 3. Photocurrent-Reverse-Bias Curves Under Uniform Excitation and Constant Absorption Condition

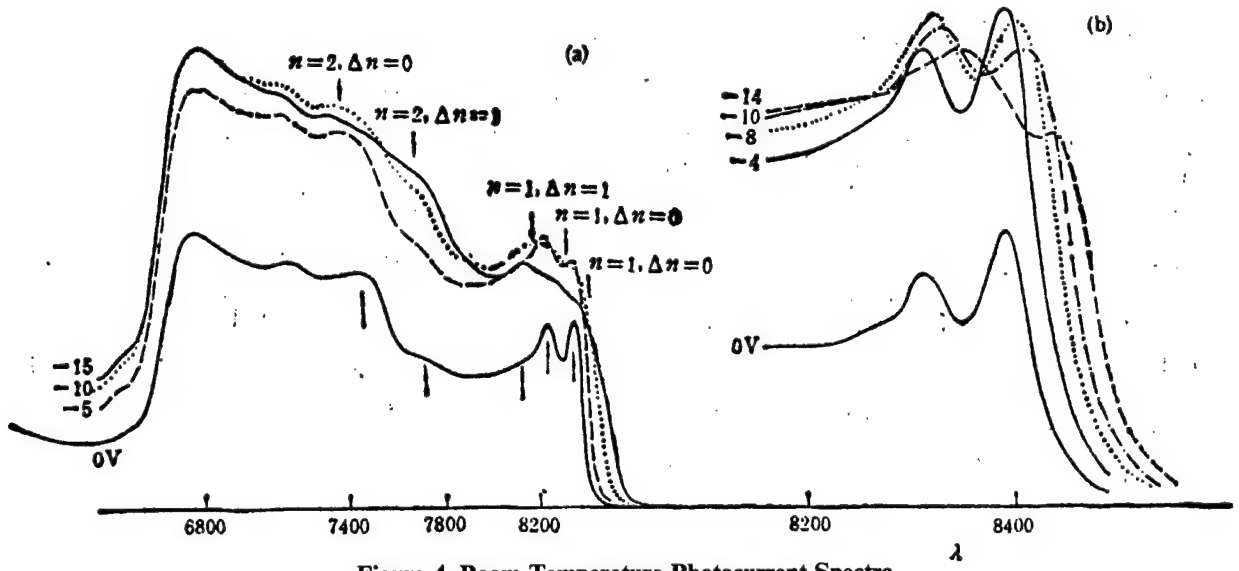

Figure 4. Room-Temperature Photocurrent Spectra

(a) 9000 Angstroms > λ > 6600 Angstroms; (b) magnified photocurrent spectra associated with light- and heavy-hole exciton absorption peaks

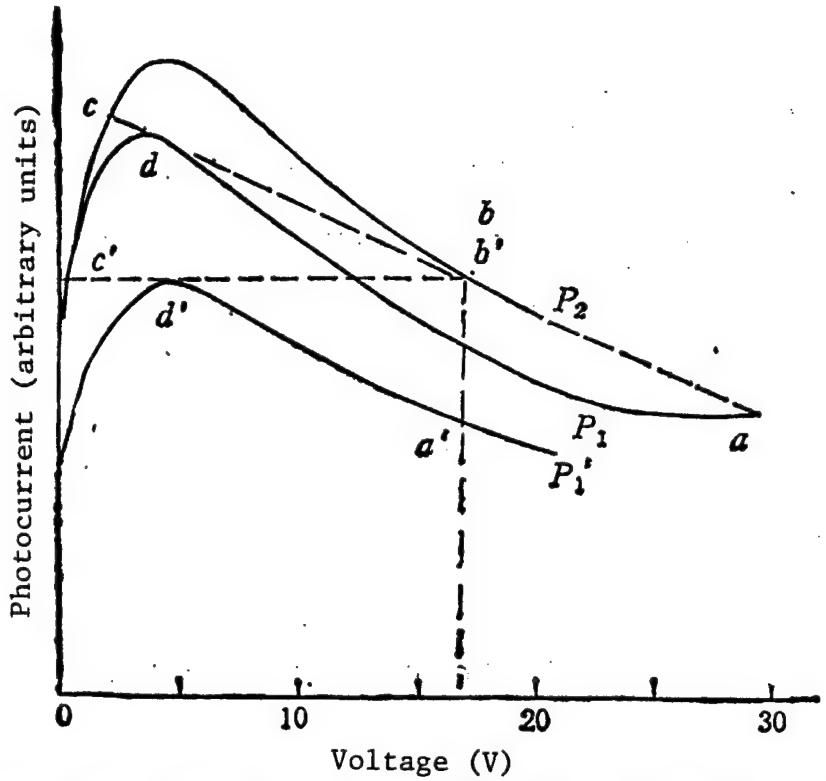

Figure 5. Optical Bistability Due to Self Electro-Optic Effect (The load is either a photodiode or a resistor.)

4. With regard to the LH1(HH1)-CB2 transition with n = 2, $\Delta n = 1$, it shifts toward shorter wavelength with increasing electric field. However, the transition intensity goes up significantly.

These experimental results are in good agreement with the qualitative theoretical analysis done by Xia Jianbai [1115 1696 4101] and Huang Kun [7806 2492].[5] Furthermore, they show that this material of large periodicity grown by our institute is structurally perfect and homogeneous.

In practical application, the electric field behavior in the light- and heavy-hole exciton absorption regions at the lowest quantum energy level is of most interest. The following section will address this issue.

IV. Self Electro-Optic Effect and Optical Bistability

Placing a MQW pin device in an external circuit in which positive electric field feedback may occur due to photocurrent (such as series-connected resistors, optical diodes, constant-current sources, etc.) would result in electro-optic switching and bistability due to the self electro-optic effect. Figure 5 shows some test results. The sample used has type-3 characteristics shown in Figure 3. From Figure 4, when the incident wavelength is on the short-wavelength side of the ground-state exciton absorption peak (n = 1) with a high bias, photocurrent versus bias curves with positive and negative slopes, as shown in Figure 5, can be obtained. Within a fixed range of voltage bias, photocurrent increases with increasing light intensity. Moreover, it causes the pin voltage distributed over the MQW device to fall, which results in increased absorption and further increases in photocurrent. Then, the pin voltage drops further until the incident wavelength coincides with the highest exciton absorption point which is limited by the external circuit. In Figure 5, considering two different incident-light sources ($P_2 > P_1$), when light intensity goes up from P_1 to P_2, the point of operation of the device jumps from b to c. Correspondingly, the photocurrent jumps as well. When light intensity falls, it operates at d instead of c. As photocurrent decreases further, until incident light intensity is reduced to P_1, the point of operation jumps from d to a. Correspondingly, the photocurrent jumps down. Thus, abcd forms a hysteresis loop which is characteristic of electro-optic bistability. In actual measurement, in order to avoid electrical breakdown of the SEED due to high reverse bias, a photodiode of a fixed intensity is used as a load in the circuit. Its load curve is shown as the right-angle curve in Figure 5. In this case, the reverse bias of the device can be greatly reduced. The bistable loop is formed by a'b'c'd'. Figure 6 [photograph not reproduced] shows the actual measured result. Section c'd' is "shorted." Because the photodiode is equivalent to a constant-current source, the output is constant for a short.

It is worthwhile to point out that the bistable photocurrent hysteresis loop caused by the self electro-optic effect is counterclockwise and that of transmitted light output is clockwise. The results of transmitted light output bistability caused by incident light will be published in the near future.

In conclusion, we have successfully developed a GaAs/GaAlAs MQW pin-structure SEED device. This paper primarily discusses its electro-optic characteristics and electro-optic bistable switching effect. The measured photocurrent spectra showed that in order to realize bistability, it is necessary for the ground-state exciton to have a red shift and a reduced transition intensity and for the device to have a d changing from less than W to greater than W within a specific bias range.

The authors sincerely thank all the people in the MBE group, the processing group in the 7th laboratory and the optical bistability group for their assistance and support.

References

1. D. A. B. Miller, D. S. Chemla, T. C. Damen, A. C. Gossard, W. Wiegmann, T. H. Wood, and C. A. Burrus, PHYS. REV. LETT., 53, 2173 (1984).

2. D. A. B. Miller, D. S. Chemla, T. C. Damen, A. C. Gossard, W. Wiegmann, T. H. Wood, and C. A. Burrus, PHYS. REV., 32, 1043 (1985).

3. I. Bar-Joseph, G. Sucha, D. A. B. Miller, D. S. Chemla, B. I. Miller, and V. Koren, APPL. PHYS. LETT., 52, 51 (1988).

4. D. A. B. Miller, D. S. Chemla, T. C. Damen, T. H. Wood, C. A. Burrus, A. C. Gossard, and W. Wiegmann, IEEE J. QUANT. ELECTRON,, QE-21, 1462 (1985).

5. Xia Jianbai and Huang Kun, WULI XUEBAO [ACTA PHYSICA SINICA], 37, 1 (1988).

Interferometric Autocorrelation Measurements of Subpicosecond Optical Pulses From 1.3-Micron-Wavelength InGaAsP Diode Laser

91FE0050B Beijing BANDAOTI XUEBAO [CHINESE JOURNAL OF SEMICONDUCTORS] in Chinese Vol 11 No 9, Sep 90 pp 674-679 [MS received 22 Sep 89]

[Article by Jia Gang [6328 0474], Sun Wei [1327 0251], Yi Maobin [5902 5399 2430], and Gao Dingsan [7559 7844 0005] of Department of Electronic Science, Jilin University, Changchun: "Interferometric Autocorrelation Measurements of Subpicosecond Optical Pulses From 1.3-μm-Wavelength InGaAsP Diode Laser"]

[Text] **Abstract**

An interferometric autocorrelator has been built using a stepper motor scanner. It was used to measure a 0.45-ps light pulse generated by a 1.3-micron InGaAsP laser. Based on interferometric autocorrelation, the pulses are unchirped secant hyperbolic pulses.

Key words: interferometric autocorrelation, InP/InGaAsP laser, ultrashort light pulse, chirp.

I. Introduction

An intensity autocorrelation system[1] is often used to measure ultrashort 1.3-micron-wavelength light pulses generated by semiconductor lasers. Through measurement of the autocorrelation function, the width of the ultrashort pulse can be indirectly determined. However, because an intensity autocorrelation system scans at a fast speed, the fast correlation term in the second harmonic signal is averaged out to 0. Therefore, the phase or frequency information contained in the fast correlation term is completely lost. Results of an intensity autocorrelation measurement cannot provide any information associated with phase or frequency. If the accuracy of optical elements in the optical autocorrelation system is very high and the scan speed is sufficiently low, the fast correlation term in the second harmonics can then be detected. This then becomes an interferometric autocorrelation system. In the past, scanning was done either pneumatically[2] or piezoelectrically[3] for an interferometric system. In the present project, for the first time, a Michelson interferometer for teaching use with a stepper motor scanner is used to measure the interferometric autocorrelation function of ultrashort pulses generated by a 1.3-micron InGaAsP laser.

II. Measurement Principle

The interferometric autocorrelation apparatus developed is shown in Figure 1. It belongs to a common-line interferometric autocorrelation measurement system with background. The incident light pulse is split into two beams by the Michelson interferometer. They are then transmitted along the same axis after being reflected by mirrors. By adjusting the position of the mirrors, the two beams have a relative time delay. By continuously adjusting the position of the mirror, it is possible to scan a series of pulses with respect to another series of pulses.

For ease of explanation, assume the electric field of light reflected by a mirror reaching a non-linear crystal at time t is E(t) and the electric field of light reflected by the movable mirror with a time delay τ is E(t-τ). In complex form, they can be expressed as:

$$E(t) = A(t)e^{i[\omega t+\phi(t)]} \quad (1)$$

$$E(t-\tau) = A(t-\tau)e^{i[\omega(t-\tau)+\phi(t-\tau)]} \quad (2)$$

where ω is the light frequency, φ(t) is the phase variation of the light pulse, and A(t) is the envelope of the light pulse electric field. Here, conditions $|dA(t)/dt| < \omega$ and $|d\varphi(t)/dt| < \omega$ are met. Thus, A(t) can be defined as the envelope. The two series of pulses reaching the non-linear crystal surface are recombined and the electric field is the sum of the two:

$$E^{\omega}(t,\tau) = E(t) + E(t-\tau) \quad (3)$$

Based on the principle of generation of second harmonic waves in non-linear optics, when phase-matching conditions are satisfied, light incident upon the non-linear crystal at frequency ω can be effectively converted to light with a frequency 2ω. This non-linear crystal is a frequency doubler. The electric field of the emitted

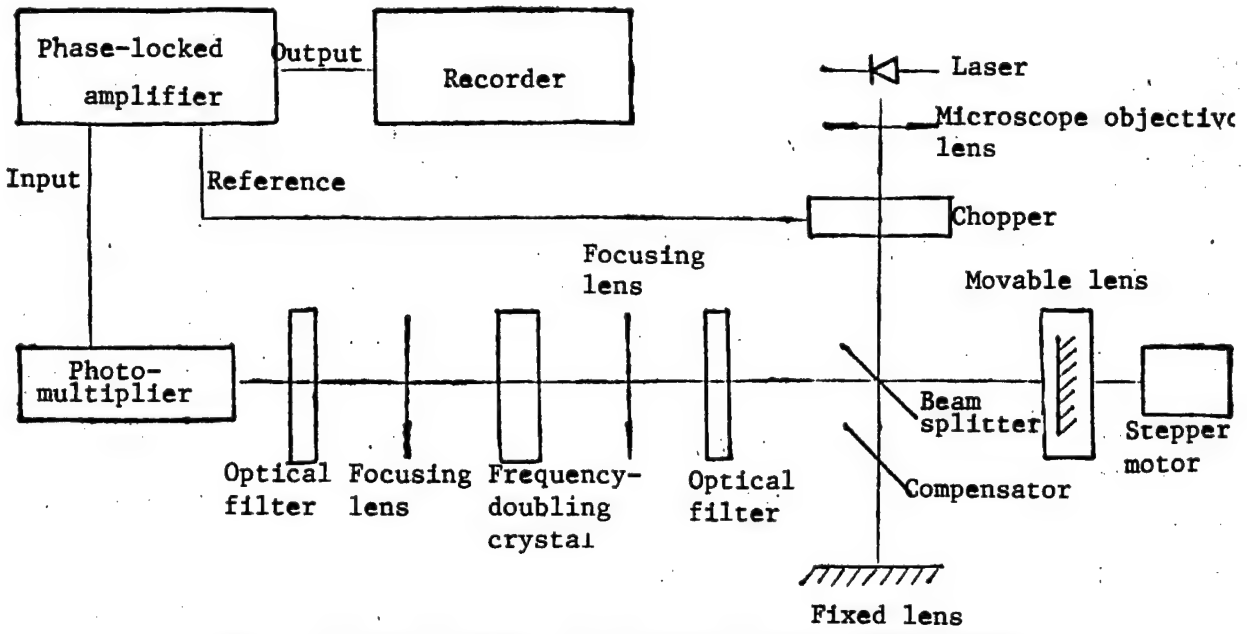

Figure 1. Schematic Diagram of the Interferometric Autocorrelation Apparatus

frequency-doubled light is proportional to the square of the electric field of the incident fundamental-frequency light:

$$E^{2\omega}(t,\tau) = d[E^{\omega}(t,\tau)]^2 \qquad (4)$$

where d is a constant dependent upon the frequency doubler. Of course, the electric field is a vector and the non-linear coefficient is a tensor. This has already been simplified in order to obtain a clear answer, and the simplification has no impact on the result. The detector used is a slow detector relative to the light pulses. The signal detected is an integration of signals. Compared to the width of the light pulse, the response time of the detector can be considered to be infinite. Therefore, the second harmonic signal measured is

$$I(\tau) = \int_{-\infty}^{\infty} \frac{D}{2} [E^{2\omega}(t,\tau)][E^{2\omega}(t,\tau)]^* dt \qquad (5)$$

where D is a constant related to the detector. Based on (1), (2), (3), and (4), equation (5) can be changed to:

$$\begin{aligned} I(\tau) = \frac{D}{2} d^2 \int_{-\infty}^{\infty} \{ & A^4(t) + A^4(t-\tau) \\ & + 4A^2(t)A^2(t-\tau) + 4[A^2(t) \\ & + A^2(t-\tau)]A(t)A(t-\tau)\cos[\omega\tau \\ & + \phi(t) - \phi(t-\tau)] \\ & + 2A^2(t)A^2(t-\tau)\cos 2[\omega\tau + \phi(t) \\ & - \phi(t-\tau)]\} dt \end{aligned} \qquad (6)$$

For convenience, a normalized second-order interferometric autocorrelation function g(τ) is introduced:

$$g(\tau) = \frac{I(\tau)}{\frac{D}{2} d^2 \cdot 2\int_{-\infty}^{\infty} A^4(t)dt} \tag{7}$$

i.e.,

$$g(\tau) = 1 + 2G(\tau) + F(\tau) \tag{8}$$

where

$$G(\tau) = \frac{\int_{-\infty}^{\infty} A^2(t)A^2(t-\tau)dt}{\int_{-\infty}^{\infty} A^4(t)dt} = \frac{\int_{-\infty}^{\infty} I(t)I(t-\tau)dt}{\int_{-\infty}^{\infty} I^2(t)dt} \tag{9}$$

$$F(\tau) = \int_{-\infty}^{\infty} \{2[A^2(t) + A^2(t-\tau)]A(t)A(t-\tau)\cos[\omega\tau + \phi(t) - \phi(t-\tau)] + A^2(t)A^2(t-\tau)\cos 2[\omega\tau + \phi(t) - \phi(t-\tau)]\}dt \Big/ \int_{-\infty}^{\infty} A^4(t)dt \tag{10}$$

From equation (8), g(τ) is normalized to background level, i.e., g(∞) = 1. In addition, from equation (9) we can see that the intensity autocorrelation function G(τ) is also normalized, i.e., normalized to peak value:

$$G(0) = 1$$

The last term F(τ) in (8) is the fast correlation term, it varies rapidly with τ. Because it depends upon ωτ and 2ωτ, a slight change in τ can average it out to 0. If the wavefront of the interfering beam is not sufficiently smooth, this term can also be easily averaged to 0. Therefore, the signal contained in this term is not easily detectable by the ordinary scanning correlation system. Usually, what we measure is the sum of the first two terms:

$$s(\tau) = 1 + 2G(\tau) \tag{11}$$

s(τ) may also be called an intensity autocorrelation function with background. In addition, it is also normalized to the background level, i.e., s(∞) = 1. s(τ) is also called the intensity autocorrelation function for short. The peak-to-background ratio of the s(τ) curve, i.e., contrast, is 3:1.

$$s(0) \text{ over } s(\infty) = 3 \text{ over } 1 \tag{12}$$

If the accuracy of optical elements is very high and scan speed is sufficiently low, this fast correlation term F(τ) can be detected. Therefore, the interferometric autocorrelation function g(τ) can be measured. The peak-to-background ratio of g(τ), i.e., contrast, is 8:1.

$$g(0) \text{ over } g(\infty) = 8 \text{ over } 1 \tag{13}$$

In order to further demonstrate the difference between interferometric autocorrelation g(τ) and intensity autocorrelation s(τ), the following is a comparison using a series of linearly chirped Gaussian pulses as an example. The electric field of these pulses is

$$E(t) = Ae^{-\frac{t^4}{2T^2}} e^{i\left(\omega t + \frac{at^4}{T^2}\right)} \tag{14}$$

where A is the peak pulse electric field, T is a constant related to pulse width, and a is a constant representing linear modulation phase shift. Substituting equation (14) into (8), we get

$$g(\tau) = 1 + 2e^{-\frac{\tau^4}{2T^2}} + 4e^{-\frac{(3+4a^2)\tau^4}{8T^2}} \cos(\omega\tau)\cos\left(\frac{a\tau^2}{2T^2}\right) + e^{-\frac{(1+4a^2)\tau^4}{2T^2}}\cos(2\omega\tau) \tag{15}$$

and

$$s(\tau) = 1 + 2e^{-\frac{\tau^4}{2T^4}} \tag{16}$$

From equation (16) we can see that s(τ) does not contain a. This means that s(τ) remains the same no matter whether pulses are chirped or unchirped. Information on phase or frequency is lost. However, from equation (15) we can see that g(τ) contains a. This means that the modulation shift in the pulses is reflected in g(τ). g(τ) includes phase or frequency information. For chirped pulses, from cos(ωτ) = cos(2ωτ) = 1, g(τ) is:

$$1 + 2e^{-\frac{\tau^4}{2T^2}} + 4e^{-\frac{(3+4a^2)\tau^4}{8T^4}} \cos\left(\frac{a\tau^2}{2T^2}\right) + e^{-\frac{(1+4a^2)\tau^4}{2T^2}} \tag{17}$$

This corresponds to maximum interference. When τ = 0, g(τ) is 8. Afterward, a maximum occurs in every optical cycle to form an upper envelope. From cos(ωτ) = -cos(2ωτ) = -1, g(τ) is:

$$1 + 2e^{-\frac{\tau^4}{2T^4}} - 4e^{-\frac{(3+4a^2)\tau^4}{8T^4}} \cos\left(\frac{a\tau^2}{2T^2}\right) + e^{-\frac{(1+4a^2)\tau^4}{2T^2}} \tag{18}$$

which corresponds to minimum interference. As τ increases or decreases from 0 by a half optical cycle, a minimum close to 0 occurs to form the lower envelope. When the time delay exceeds the pulse correlation time, upper envelope and lower envelope combine into a curve that coincides with the intensity autocorrelation curve. If there is no modulation shift, i.e., a = 0, then the upper and lower envelope of $g(\tau)$ are:

$$1 + 3e^{-\frac{\tau^2}{2T^2}} + 4e^{-\frac{3\tau^2}{8T^2}} \qquad (19)$$

and

$$1 + 3e^{-\frac{\tau^2}{2T^2}} - 4e^{-\frac{3\tau^2}{8T^2}} \qquad (20)$$

respectively. Therefore, the envelope of $g(\tau)$ apparently can reflect whether pulses are chirped. When a = 0, 0.5, and 1, the envelopes of $g(\tau)$ are calculated and shown in Figure 2. Figure 2 indicates that the envelope of $g(\tau)$ varies with a. This illustrates that $g(\tau)$ contains phase or frequency information.

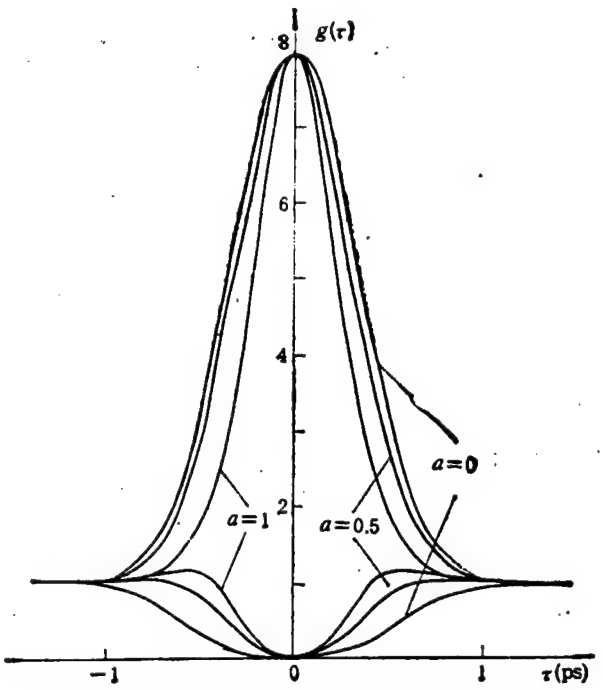

Figure 2. Theoretical g() Envelopes of 0.5-ps Half-Width Light Pulses When a = 0, 0.5, and 1

III. Measurement Apparatus

The interferometric autocorrelation measurement system developed is a second-order harmonic autocorrelation interferometer with background. The block diagram of the device is shown in Figure 1. The 1.3-micron-wavelength semiconductor laser beam is collimated by a microscope before entering a modified Michelson interferometer. Wave chopping is used for phase-locked amplification of the electrical signal. The beam is split by a 1/2:1/2 beam splitter into two beams. One beam is reflected to the variable-delay arm of the interferometer. The movable mirror in this arm is driven by a stepper motor. After being reflected by the movable mirror, it is transmitted through a beam splitter. In order to ensure that the fast correlation term can be measured, the step of the movable mirror must be less than one-tenth that of the wavelength. The time interval between two steps must be long enough for the phase-locked amplifier to accurately measure the signal. The other beam passes through a compensator before reaching the mirror in the fixed arm. After getting reflected by the mirror, it returns to the beam splitter and is reflected to the output. The two ultrashort pulses are recombined and propagate along the same axis. In order to ensure that the wavefronts of these two beams are smooth, the flatness of these two mirrors is better than one-fiftieth of the wavelength. Then, the combined light beam goes through a filter to remove 650-nm-wavelength light from the frequency-doubled light of the laser. This beam is then focused on a frequency doubler which is made of lithium iodate crystal. The matching angle is between 24 and 25 degrees. In order to prevent the deliquescent effect, the frequency doubler is sealed in a desiccator. The frequency-doubled light is again focused by lens and the fundamental-frequency 1.3-micron light is removed by a filter. Finally, a photomultiplier is used to receive the second-harmonic-wave signal. A phase-locked amplifier is used to measure the electrical signal. A recorder is used to record the interferometric autocorrelation $g(\tau)$ curve. The optical path of the entire system is first aligned by a He-Ne laser. Afterward, because the system is optically shielded, it may be adjusted to its optimum operating condition with light on. Therefore, it has high sensitivity and resolution.

IV. Measurement Results

We used this interferometric autocorrelation instrument to measure subpicosecond light pulses from a 1.3-micron InGaAsP laser. When the light delay is close to 0, direct observation was made with an image converter tube at the output end of the Michelson interferometer. The light spot was found to vary periodically with the optical cycle. Measurement was then made at the output of the interferometric autocorrelation device. The curve measured is shown in Figure 3. It clearly shows that maximum and minimum interference vary periodically with the optical cycle. Figures 4 and 5 show the middle part of the subpicosecond 1.3 micron laser pulses measured by the intensity autocorrelation system and interferometric autocorrelation system, respectively. The dots in Figure 4 are the calculated values of the intensity autocorrelation function based on secant hyperbolic pulses. The outer profile in Figure 5 is the upper and lower envelope of the interferometric autocorrelation function calculated based on unchirped hyperbolic secant pulses. Based on the fit of the intensity autocorrelation curve, the light pulse is a hyperbolic secant envelope and the half width

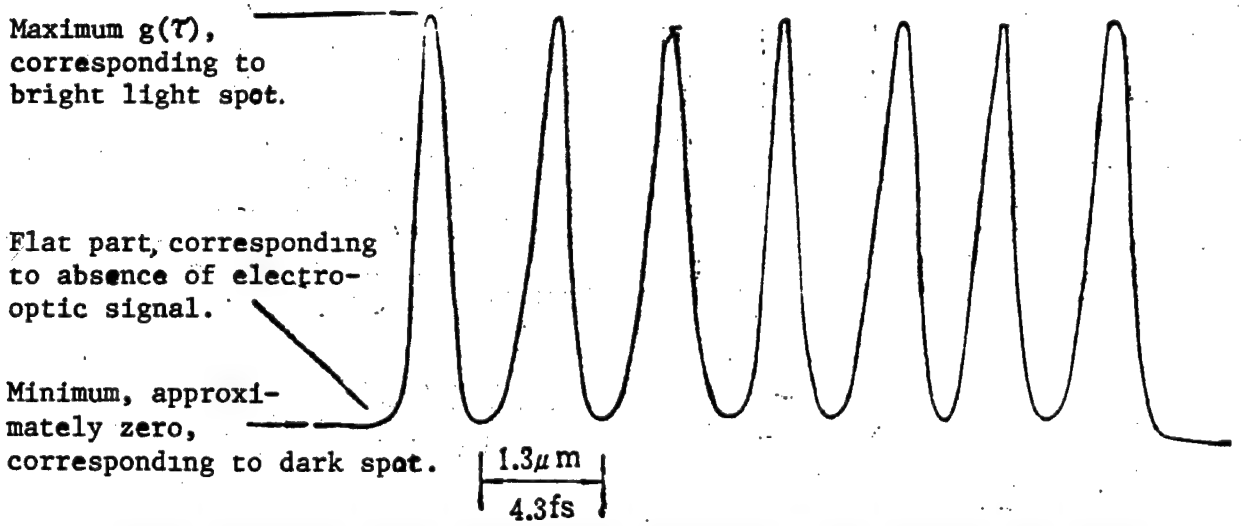

Figure 3. Experimental Curve of Interferometric Autocorrelation Function Near Zero Time Delay

is 0.45 picosecond. As far as we know, this is the shortest light pulse generated by a semiconductor laser. A separate paper will report the generation of this ultrashort light pulse. Based on the fit of the interferometric autocorrelation curve, it is determined to be an unchirped hyperbolic secant pulse. As far as this conclusion is concerned, only interferometric autocorrelation can arrive at this statement. It cannot be obtained from intensity autocorrelation because it does not contain any phase information.

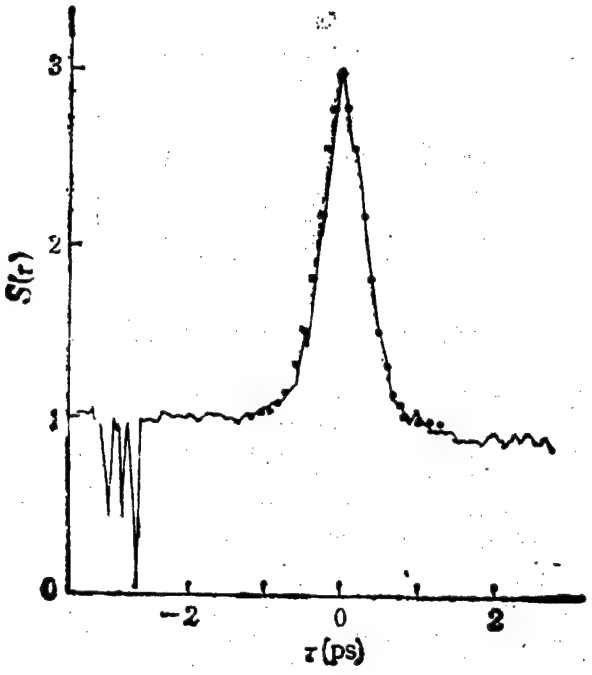

Figure 4. Intensity Autocorrelation Function

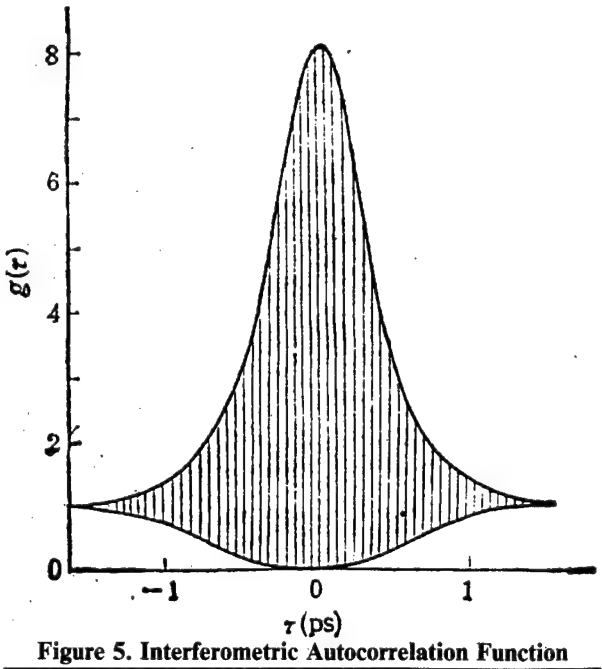

Figure 5. Interferometric Autocorrelation Function

References

V. Conclusions

An interferometric autocorrelation system using a stepper motor scanner has been developed. It was successfully used to measure the shortest light pulse generated by an InGaAsP laser. Based on curve fitting, it was determined that this pulse was a 0.45-ps unchirped hyperbolic secant light pulse.

1. N. Onodera, H. Ito, and H. Inaba, IEEE J. QUANTUM ELECTRON., QE-21, 568 (1985).

2. J. C. Diels, E. W. Van Stryland, and D. Gold, "Picosecond Phenomena," eds. C. V. Shank, S. L. Shapiro, and E. P. Ippen, 117, Springer-Verlag (1978).

3. T. Kurobori, Y. Cho, and Y. Matruo, OPTICS COMMUN., 40, 156 (1981).

High-T_c Oxide Granular Superconductor Current-Injection Three-Terminal Devices Fabricated, Studied

91FE0118B Beijing DIANZI XUEBAO [ACTA ELECTRONICA SINICA] in Chinese Vol 18 No 5, Sep 90 pp 124-126 [MS received May 89, revised Nov 89]

[Article by Tang Zudun [3282 4371 1908] and Jiang Jianfei [5592 1696 7378] of the LSI Research Center, Shanghai Jiaotong University: "Experimental Studies of Current-Injection Three-Terminal Devices of Type B Made From High-T_c Oxide Superconductor"]

[Text] Abstract

The characteristics of a Type-B high-T_c [critical temperature], oxide granular superconductor current-injection three-terminal device, B-HOGSCITTD, and its necked-down version, NB-HOGSCITTD, are experimentally studied. The results show the possibility of using such structures for switches and amplifiers. It was found that B-HOGSCITTD and NB-HOGSCITTD have similar characteristics, which further indicates the granularity and weak linkage of such high-T_c oxide superconductors.

I. Introduction

The feasibility and relevant analysis of high-T_c oxide granular superconductor current-injection three-terminal devices (HOGSCITTD) were presented in references [1] and [2]. The multi-terminal weak-link dc V-I curve and granular superconductivity of the superconductor YBaCuO were reported in references [3] and [4]. On the basis of these studies and the work of other researchers, the characteristics of B-HOGSCITTD and NB-HOGSCITTD[1] are experimentally studied in this work. Our results show that both devices have basic characteristics similar to switching and amplification.

II. Device Structure

Figures 1 (a) and (b) show the structures of these two devices. The material used is YBaCuO with T_c = 90 K. They were polished and hand carved. B-HOGSCITTD consists of three long strips connected by a common area O. The dimensions are $L_{10} = L_{20} = L_{30} = 1$ cm. The width W is 0.2 cm and thickness δ is 0.5 mm. NB-HOGSCITTD consists of three reduced-neck bridges connected by a common area O. The dimensions are that each bridge length L is 1.5 cm, width W is 0.5 cm, thickness δ is 0.2 cm. The neck is 0.2 x 0.2 x 0.2 cm.

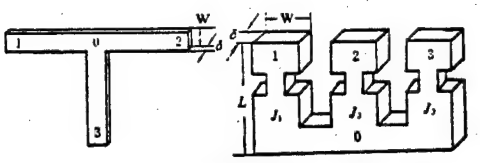

Figure 1. Device Structures (left: B-HOGSCITTD, right: NB-HOGSCITTD)

III. Experimental Method and Results

A double-bias circuit, as shown in Figure 2, was used in the experiment. The dotted block is the device to be tested. During testing, a standard four-wire method separating lead wires for current and voltage was used. The sample was immersed in liquid nitrogen.

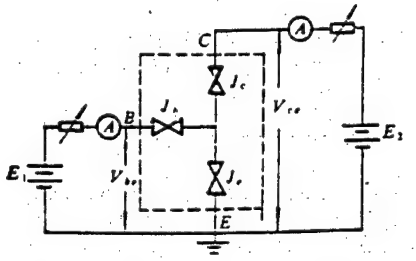

Figure 2. Test Circuit for HOGSCITTD

First, the characteristics of the B-HOGSCITTD are considered. Terminals 2-3 form the b-e circuit and 1-3 forms the c-e circuit. First, fix I_{be} at a certain number and then measure the I-V characteristics across c-e. A series of I_{ce}-V_{ce} characteristics can be obtained by changing I_{be}, as shown in Figure 3.

Use 1-3 to form the b-e circuit and 2-3 to form the c-e circuit and then fix I_{ce} and vary I_{be}. Every time I_{be} is varied, measure V_{be} and V_{ce}. Table 1 shows the results and the calculated voltage amplification factor ($\Delta V_{ce}/\Delta V_{be}$). Figure 4 shows the voltage transition relation of the two circuits.

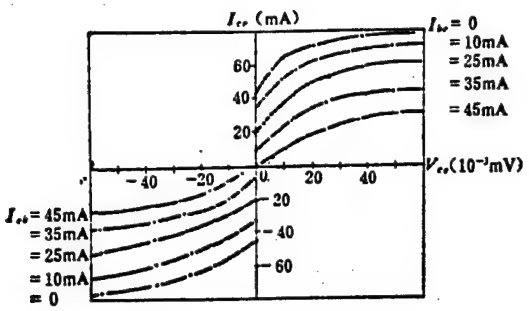

Figure 3. Transmission Characteristics of HOGSCITTD

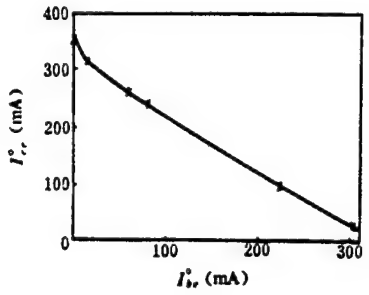

Figure 5. Current Transition Curve for NB-HOGSCITTD

Table 1. Voltage Amplification Factor of B-HOGSCITTD

I_{ce} = 50 mA

I_{be} (mA)	V_{be} (mV)	V_{ce} (mV)	$\Delta V_{ce}/\Delta V_{be}$
0	0.003	1.702	
10	0.019	1.767	4.062
20	0.056	1.818	1.378
30	0.108	1.901	1.596
40	0.213	2.011	1.048
50	0.351	2.180	1.225
60	0.586	2.421	1.026

Table 2. Voltage Amplification Factors for NB-HOGSCITTD

I_b (mA)	V_{be} (mV)	V_{ce} (mV)	$\Delta V_{ce}/\Delta V_{be}$
295	0.001	-1.331	
308	0.006	-1.382	-10.2
320	0.013	-1.458	-10.9
335	0.022	-1.542	-9.3
350	0.034	-1.650	-9.0
365	0.049	-1.758	-7.2

Next, the characteristics of NB-HOGSCITTD were investigated. Use J_2 as J_b, J_1 as J_e, and J_3 as J_c. A fixed bias current I_{ce} was applied to circuit c-e. Under this bias current, both ends of c-e were kept in a superconducting state, i.e., zero voltage at both ends of c-e. Then, the bias in the b-e circuit was varied. When I_{be} reached a certain value, there was a voltage across c-e. Figure 5 shows the I°_{ce} versus I°_{be} curve for c-e to change from zero voltage to finite voltage.

Then, use Use J_1 as J_b, J_2 as J_c, and J_3 as J_e. First, I_{be} was adjusted to a specific value to put b-e in a critical state between superconducting and normal. Then, I_{be} was varied. For every I_{be} value, measure the voltage across b-e and that across c-e. The results are shown in Table 2 and Figure 6.

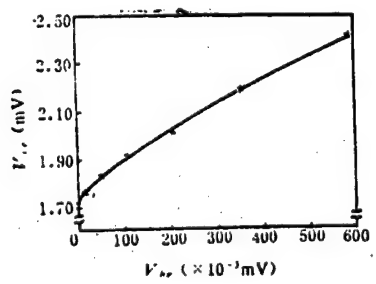

Figure 4. Voltage Transition Characteristics of B-HOGSCITTD

IV. Conclusions

From these experiments, we reached the following three conclusions:

1. From Figures 3 and 5, it is possible to switch c-e from superconducting to normal mode by adjusting the current in b-e using the test circuit shown in Figure 2. This kind of control shows that the device has a switching function.

2. From Tables 1 and 2 and Figures 4 and 6, one can see that the voltage across b-e will directly affect the voltage across c-e. Under suitable conditions, the increase in the

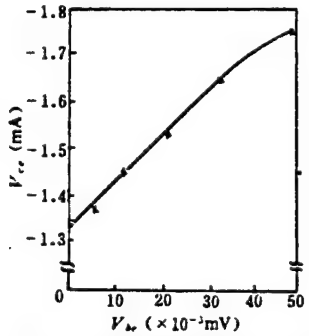

Figure 6. Voltage Transition Characteristics of NB-HOGSCITTD

voltage across c-e is larger than that across b-e. This indicates that this three-terminal device has some amplification function.

3. It was determined experimentally that B-HOGSCITTD and NB-HOGSCITTD have similar switching and amplification characteristics. This reflects the granular superconductivity and weak orderless linkage of high-T_c YBaCuO.

References

[1] Jiang Jianfei, Tang Zudun, et al., "Symposium on High-Temperature Superconductors," Shanghai, 1989, Vol 1, Shanghai Science and Technology Publ. House.

[2] J. F. Jiang and Z. D. Tang, submitted to Semiconductor and Integrated Circuit Technology International Conference, Beijing, China, Oct 89.

[3] Tang Zudun, Jiang Jianfei, et al., "Proceedings of National High-T_c Superconductor Symposium," Vol 3, p 318, Apr 88.

[4] Jiang Jianfei, Tang Zudun, et al., "Proceedings of National High-T_c Superconductor Symposium," Vol 4, p 333, Apr 88.

Achievements of CAS Optoelectronics Institute Profiled

91FE0114A Tianjin ZHONGGUO JISHU SHICHANG BAO [CHINA TECHNOLOGY MARKET NEWS] in Chinese 6 Oct 90 p 1

[Article by Zhu Yonggang [6772 6343 2504] and Deng Xianchun [4554 3057 0474]: "Achievements of CAS Optoelectronics Institute Profiled"]

[Text] The CAS Optoelectronics Institute has had a large number of achievements in the development of special microelectronic equipment. Seven out of the 15 major achievements have received technical achievement awards from CAS and the province of Sichuan. The institute has made a significant contribution to the development of microelectronics in China.

In order to meet the challenge of the new technology revolution head-on, the CAS Optoelectronics Institute has decided to make LSI special-purpose equipment development one of its research areas. To this end, a number of key people were assigned to build a new laboratory. Since 1978, they have developed a semi-automatic proximity/contact photolithographic machine, a circular electron-beam exposure-machine laser positioning platform system and a variable rectangular electron-beam exposure-machine laser positioning platform system. These systems have been used in the field, and have been given a first-place technology progress award by CAS.

In recent years, the institute has been assigned several key projects by the government, including a direct step-and-repeat projection photolithographic machine, an automatic mask-defect detection system, a synchrotron radiation X-ray lithographic machine, a laser-based instrument to detect and repair defective masks and a silicon-chip surface-defect detector. Under the difficult situation wherein there are no imported units to examine and no relevant information to refer to, after more than 6 years of hard work CAS Optoelectronics Institute solved many key technical hurdles and successfully developed a prototype direct step-and-repeat projection photolithographic machine. Currently, the resolution of the machine is 0.8 micron; within a 10x10 mm full viewing field, the practical linewidth is 1.25 microns and co-axial accuracy is 0.24 micron. It can process 39 3-inch silicon wafers per hour. For China, this machine is a technologically advanced, full-featured prototype.

Through developing special optical equipment for microelectronics, CAS Optoelectronics Institute not only has acquired a great deal of experience in integration but also laid down a good foundation for the development of special equipment for sub-micron-level microelectronics in the future.

New Magnetron RIE Equipment Developed

91FE0114C Beijing KEJI RIBAO [SCIENCE AND TECHNOLOGY DAILY] in Chinese 24 Oct 90 p 1

[Article by Guo Kun [6753 3824]: "New Magnetron RIE Equipment Developed"]

[Text] The CAS Microelectronics Center recently developed new magnetron RIE (reactive ion etching) equipment with novel magnetic circuits and a novel electrode structure. The equipment's magnetic field homogeneity is plus or minus 2 percent (3-4 inches) and its etching uniformity is plus or minus 3 percent. The etching speed is one order of magnitude higher than before, with excellent reproducibility and stability.

RIE is a key technology for fabricating integrated circuits. However, due to the low etching rate and high damage to silicon wafers associated with ordinary RIE technology, magnetron RIE technology has been developed in other countries. It primarily involves applying a magnetic field over the RIE equipment to drastically increase etching rate and decrease damage to silicon wafers. The key is to obtain a homogeneous magnetic field over a large area. Presently, IC technology is being rapidly developed; patterns are getting denser and silicon-wafer diameter is getting larger (6 inches). It is very difficult to obtain a homogeneous magnetic field for such a large area. In other countries, it is usually done by scanning with either electromagnets or permanent magnets. These methods introduce a great deal of complexity and difficulty to the fabrication equipment, as well as inconvenience in use. The novel magnetic circuit and electrode structure developed [domestically] is simple; a large homogeneous magnetic field can be obtained without scanning. Its successful development has great significance for the development of microelectronic technology in China. A patent application has been filed for this achievement.

New Test Instrument for Satellite Navigation Receivers Developed

91FE0114B Beijing KEJI RIBAO [SCIENCE AND TECHNOLOGY DAILY] in Chinese 17 Oct 90 p 2

[Article by Liu Shiguang [0491 0013 0342] and Zhao Jin [6392 6651]: "New Test Instrument for Satellite Navigation Receivers Developed"]

[Text] The first comprehensive test instrument for satellite navigation receivers in China, developed by the Chinese Naval Satellite Navigation Maintenance Center, has been found to be extremely beneficial in military, economic and social aspects after over 2 years of use.

A satellite navigation receiver is an around-the-clock, all-weather global navigation system which receives omega signals from meridian instruments on satellites. In 1988, the Chinese Naval Satellite Navigation Maintenance Center successfully developed this comprehensive test instrument for satellite navigation receivers, which has been certified by civilian and military experts. This marks the first time that onboard electronic equipment can be maintained and repaired independently in China. Satellite navigation receivers are no longer repaired by foreign agents.

Fuzzy-Relation Equation-Solving Circuit Realized with SCMAIC

91FE0118A Beijing DIANZI XUEBAO [ACTA ELECTRONICA SINICA] in Chinese Vol 18 No 5, Sep 90 pp 114-117 [MS received Mar 89, revised Dec 89]

[Article by Lin Weiping [2651 0251 1627] of South China University of Technology: "Fuzzy-Relation Equation-Solving Circuit Realized with SCMAIC"]

[Text] Abstract

In this paper, based on SCMAIC (Semi-Custom Multiple-Valued-Logic Array IC),[1] a fuzzy comparator circuit suitable for solving fuzzy-relation equations is designed. Furthermore, this comparator circuit is used as a basic array element to realize a fuzzy-relation equation-solving circuit. The system does not need any A/D conversion. It is solely based on SCMAIC and can be conveniently integrated onto one chip to realize fast fuzzy-relation equation-solving.

I. Introduction

Since its advent, the NMOS-DYL circuit,[2] because of its simple structure, fast speed and low power consumption, has received much attention. In reference [1], it was developed into a semi-custom circuit, SCMAIC, for implementing non-destructive information processing. Furthermore, it was found to have a wide range of applications in digital communications, real-time control and fuzzy automatic control. In reference [3], we explored the theoretical aspect of using fuzzy control in airplane auto-piloting. These analyses show that SCMAIC is extremely suitable for a fuzzy logic system. Based on this concept, a fast fuzzy-relation equation-solving SCMAIC circuit is presented in this paper.

II. Solving Fuzzy-Relation Equations

The fuzzy-relation equation, introduced by E. Sanchez in 1976, is useful in computer applications such as clinical diagnosis, fuzzy automatic control and artificial intelligence. Therefore, solving fuzzy-relation equations is becoming ever more important.

In a fuzzy relation, AoR = B, B and R are known and A is the unknown to solve. This is the problem of solving a fuzzy-relation equation. Among the commonly used methods to solve fuzzy-relation equations, the ideal feasible method is the "Xu, Luo, Cao and Li" method introduced in references [4] and [5]. It overcomes the low accuracy of the approximation method and the large workload of the TKM method.

Based on the "Xu, Luo, Cao and Li" method introduced in references [4] and [5], the author modified it to simplify the circuit design and scale. The first step, standardized arrangement, was eliminated. It was proven that the solution was identical. The modified steps are as follows:

Assume the fuzzy relation equation is AoR = B, all components of the known vector B are b_i, and the relation equation is $R = (r_{ji})$.

1) r_{ji}, can be found based on the following equation:

$$r_{ji}' = \begin{cases} b_i & \text{for } r_{ji} > b_i \\ 1 & \text{for } r_{ji} \leqslant b_i \end{cases} \qquad (1)$$

Then, the infimum z_i can be determined:

$$z_i = \min_{j=1}^{n} (r_{ji}') \qquad (2)$$

2) r_{ji}" can be determined by the following equation:

$$r_{ji}'' = \begin{cases} b_i & \text{for } r_{ji} \geqslant b_i \\ 0 & \text{for } r_{ji} < b_i \end{cases} \qquad (3)$$

3) Remove all elements greater than z_i from each row in the R" matrix, i.e.:

$$r_{ji}''' = \begin{cases} r_{ji}'' & \text{for } r_{ji}'' \leqslant z_i \\ 0 & \text{for } r_{ji}'' > z_i \end{cases} \qquad (4)$$

4) Determining and Solving Equation

The necessary and sufficient condition for the original equation to have a solution is that the matrix obtained in step 3) does not have a column that has all "0" elements, i.e.:

$$\overset{n}{\underset{j=1}{MAX}} r_{ij}''' \neq 0 \quad \text{or} \quad \overset{n\times n}{\underset{i=1}{MIN}} PRI_i \neq 1 \quad (5)$$

where

$$PRI_i = \begin{cases} 1 & \text{for } r_{ij}''' > z_i \\ 0 & \text{for } r_{ij}''' \leqslant z_i \end{cases} \quad (6)$$

The way to solve the equation is to choose the first non-zero element for each column in the matrix obtained in step 3), set all other elements to be 0, and then try to determine the supremum z_i':

$$z_i' = \overset{n}{\underset{i=1}{MAX}} r_{ij}''' \quad (7)$$

5) With respect to the infimum z_i and supremum z_i' obtained in steps 3) and 4), the equation has a partial set of solutions, and it is necessary to make further selection. One of the methods is to take their minimal values, i.e.:

$$a_i = z_i'' \in [z_i, z_i'] \quad \text{or} \quad a_i = \min(z_i, z_i') \quad (8)$$

III. Fuzzy-Relation Equation-Solving Circuit

1. Fuzzy Quantization Circuit

The range of fuzzy quantization is 0.0 - 3.0 V, and the level (or step) difference is 0.3 V. Therefore, there are nine fuzzy subsets, including extremely negative, highly negative, moderately negative, slightly negative, zero, slightly positive, moderately positive, highly positive and extremely positive. The SCMAIC-based fuzzy quantization circuit is shown in Figure 1. The nine fuzzy subsets are expressed by a two-digit ternary number. In the circuit, the two opening voltage levels for the threshold circuit are 0.3 V for "1" and 0.6 V for "2."

Since the triple-threshold calculating circuit is an NMOS and DYL circuit which is also located on the same silicon substrate, there is no need for an isolation island. The DYL circuit requires a lower doping level at the silicon substrate. The NMOS is fabricated by making a P well on the substrate and then diffusing two N regions on top of it. Therefore, it is possible to use ion implantation to fabricate several NMOS diodes by controlling the doping level in the P well. In practice, it is not difficult to fabricate NMOS diodes with a low activating voltage. Figure 2 [photograph not reproduced] shows the experimental results of the circuit. The triple-threshold calculation circuit used in the experiment is a special dual-threshold IC LT1 provided by Foshan Radio Factory

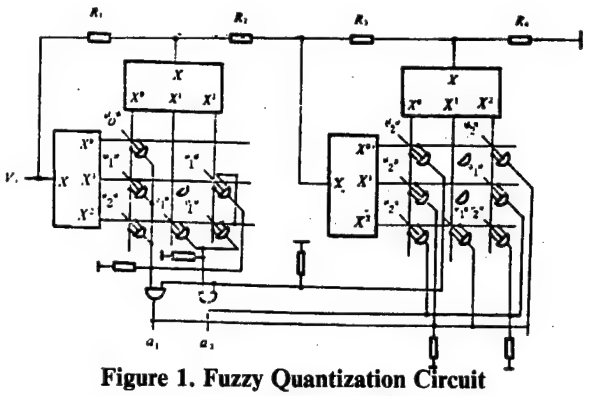

Figure 1. Fuzzy Quantization Circuit

Number 4 in Guangdong Province. The two unblocked levels are 2.5 and 3.5 V, respectively; therefore, full-scale output is obtained at 10 V input. A low-unblocked-level triple-threshold calculating circuit is yet to be developed in collaboration with an IC manufacturer. At the present moment, the quantization rate is 5 MHz.

2. Fuzzy Comparator Circuit

In order to realize operations in equations (1), (3), (4) and (6), we used SCMAIC to materialize the comparator circuit. Moreover, it is combined with the fuzzy quantization circuit described earlier to form a fuzzy comparator circuit. A fuzzy number is quantized by the fuzzy quantization circuit to become a two-digit ternary number to be compared with the quantized fuzzy number. Let us assume that the quantized value of r_{ji} is r_2r_1 and the quantized value of b_i is b_2b_1, where r_2 and b_2 are the higher digits. Then, the logic expressions for comparison are:

$$\begin{aligned}(r_{ij} < b_i) &= (r_1^0 \cdot b_1^1 + r_1^0 \cdot b_1^2 + r_1^1 \cdot b_1^2) \\ &\quad \cdot (r_2^0 \cdot b_2^0 + r_2^1 \cdot b_2^1 + r_2^2 \cdot b_2^2) \\ &\quad + (r_2^0 \cdot b_2^1 + r_2^0 \cdot b_2^2 + r_2^1 \cdot b_2^2) \\ (r_{ij} > b_i) &= (r_1^1 \cdot b_1^0 + r_1^2 \cdot b_1^0 + r_1^2 \cdot b_1^1) \\ &\quad \cdot (r_2^0 \cdot b_2^0 + r_2^1 \cdot b_2^1 + r_2^2 \cdot b_2^2) \\ &\quad + (r_2^1 \cdot b_2^0 + r_2^2 \cdot b_2^0 + r_2^2 \cdot b_2^1) \\ (r_{ij}'' \leqslant z_i) &= \overline{r_{ij}'' > z_i} = \overline{PRI_i}\end{aligned}$$

The comparator circuit realized based on above equations and method is shown in Figure 3. The two activating voltage levels for the triple-threshold circuit are 2.5 V and 3.5 V. The fuzzy comparator circuit is made by connecting the outputs of two fuzzy quantization circuits to the input of a comparator circuit. In addition, because the PRI_i expression for r_{ji}', r_{ji}'' and r_{ji}''', respectively. For simplicity, only one expression is used; it is shown in Figure 4.

3. Fuzzy-Relation Equation-Solving Circuit

Using the fuzzy comparator circuit shown in Figure 4 as an array element, based on the above algorithm and logic

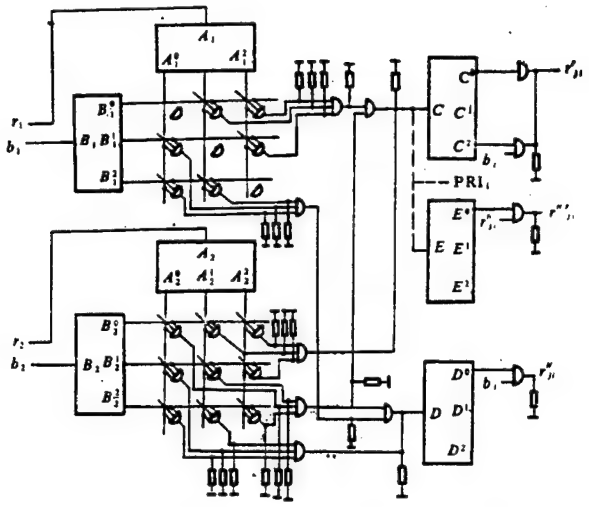

Figure 3. Comparator Circuit—Note: All unmarked inputs of DYL and the gates are connected to voltage level "z."

expressions, a fuzzy-relation equation-solving circuit, as shown in Figure 5, is realized. In Figure 5, the first non-zero element in each column is chosen by a prioritizing circuit. Then, this array circuit is used to solve the fuzzy-relation equation. Its delay time is only the delay at several gates, usually less than 1 microsecond. If a microcomputer is used to solve this equation with assembly language, over a hundred lines of codes are required based on the method described. Each command takes approximately 1-2 microseconds. Therefore, this equation-solving circuit is at least two orders of magnitude faster than using software.

IV. Conclusions

In this work, a fuzzy-relation equation-solving circuit using a fuzzy comparator circuit as an array element is designed. It has a high solving speed. In addition, the system is designed based on SCMAIC technology which makes it feasible to realize a low-cost single-chip fuzzy-relation equation-solving circuit. The use of SCMAIC in

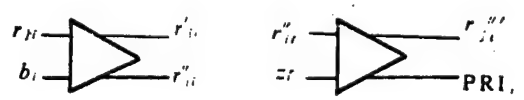

Figure 4. Expression for Fuzzy Comparator Circuit

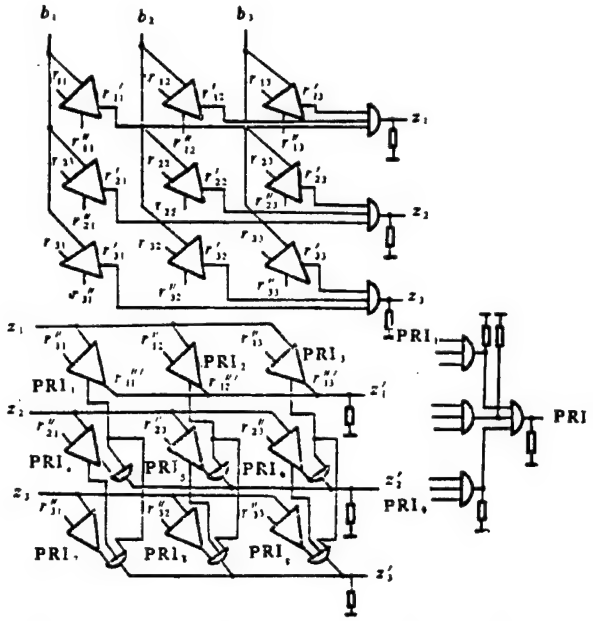

Figure 5. Fuzzy-Relation Equation-Solving Circuit

a fuzzy-logic decision-making circuit and a fuzzy-relation equation-solving circuit has been proven and realized. It is projected that SCMAIC has a bright future in fuzzy information processing technology with more in-depth research.

References

[1] Lin Weiping, Zhang Qilun, and Huang Guanguang, "A Semi-Custom Technique Realizing Non-Destructive Information Processing," Proceedings of ISMVL 88, pp 45-50, 1988.

[2] Huang Zhihai [7806 1807 3189], Zheng Qilun [6774 0796 0243], and Huang Guanguang [7806 3606 0342], "MOS/DYL-Compatible Multiple-Valued-Logic Circuit," DIANZI XUEBAO [ACTA ELECTRONICA SINICA], Vol 13 No 5, pp 1-7, 1985.

[3] Sun Boming [1327 0130 2494], Lin Weiping, and Zheng Qilun, "Fuzzy Control in Auto-Piloting of an Airplane," Proceedings of the Second National Multiple-Valued-Logic Symposium," Chongqing, China, Mar 1987.

[4] He Zhongxiong [6320 0112 7160], "Fuzzy Mathematics and Its Applications," first edition, Tianjin Science and Technology Publishing House, 1984.

[5] Wang Peizhuang [3076 1014 8369], "Fuzzy Set Theory and Its Applications," first edition, Shanghai Science and Technology Publishing House, 1984.

Chinese Physicists Comment on Cold Fusion Developments

91FE0130A Beijing BEIJING KEJI BAO [BEIJING SCIENCE AND TECHNOLOGY NEWS] in Chinese 20 Oct 90 p 1

[Text] An academic exchange and strategy meeting on cold fusion was recently organized by the Chinese Nuclear Physics Society and the Low Energy Nuclear Physics Institute of the Beijing Normal University. Famous Chinese scientists including Wang Ganchang [3769 3227 2490] and Peng Huanwu [1756 2719 2976] were invited.

During the meeting, participating scientists conducted rigorous evaluation of cold fusion research in the world and reported on their own progress. Based on the spirit of unbiased open discussion, the scientists expressed their opinion on the present problems in cold fusion and its future prospects.

Judging from the reports of the scientists, there are now three views in China on cold fusion: 1) it has application potential as an energy source, 2) it is unrelated to nuclear power sources, and 3) based on currently available experimental results, there has not been sufficient evidence to show that cold fusion is related to nuclear power. However, unusual phenomena have their scientific value, especially when the phenomenon involves systems spanning four orders of magnitudes from solid lattices, to atoms, molecules and nuclei. An in-depth study of the phenomenon may lead to new understanding of energy, material and nuclear reactions. For this reason, cold fusion should receive a proper level of support. Despite some differences in approach and emphasis, there was a consensus among the scientists regarding the research of cold fusion in China. It was generally believed that (1) China has sufficient technological resources to follow the trend of international research, (2) Chinese scientists have new ideas and are exploring specific phenomena, and (3) due to the complexity and specialty of the cold fusion phenomenon, the background ratios of the experiments are low and there has not been reproducible experiments; considerable more work is required to verify the experiments.

Based on these understanding, scientists of the Chinese Nuclear Physics Society made the following recommendations to the state S&T administration:

1. The "cold fusion" phenomenon should be regarded as a natural phenomenon worthy of further investigation. The state should allocate support for the 1990-1992 period and establish a "speculative" basic research project to study cold fusion.

2. Select a few highly qualified laboratories to start the experimental work. Select one or two laboratories to build up a multi-parameter instrumentation capable of measuring the neutrons, tritium, gamma ray or x-ray in Jones' experiment so that a definitive conclusion may be reached.

3. Provide appropriate support to researchers with novel ideas.

4. Support a few solid state studies with clearly defined goals and objectives.

5. The experiments should gradually shift from phenomenological studies to intrinsic studies; however, under the present funding level, the first task is still to the establishment of the phenomenon.

6. Organize experts in China, include specialists in nuclear physics, condensed matter physics, electrochemistry, materials science, and metrology, to form an expert group of experimentalists and theorists, of enthusiastic supporters as well as nonbelievers to evaluate and understand the progress of cold fusion research in China.

7. Depending on developments in China and abroad, timely adjustments of this policy should be made. Attention should be given to the collection of technical data from abroad and to the enhancement of academic exchange, in the form of scientific meetings.

Controlled Fusion Research Update

91FE0130B Beijing BEIJING KEJI BAO [BEIJING SCIENCE AND TECHNOLOGY NEWS] in Chinese 30 Oct 90 p 1

[Article by Zhao Xiaoyan [6392 1420 3601]]

[Text] After 5 years of operation and experiments, China's largest controlled fusion facility—the HL-1—has produced important results. The apparatus and the experimental capability are among the most advanced as compared to similar facilities in the world. On 25 October, research results of the circulator No. 1 were accredited by the Chinese General Nuclear Power Company in a meeting held at the Southwest Physics Institute.

Nuclear fusion research is the only important approach to a permanent solution of the energy problem. It involves many disciplines in high technology and attracted wide attention of all the countries in the world. Based on a tradition of self-reliance and working under difficult conditions, researchers in the Southwest Physics Institute designed the Chinese HL-1 on their own. The apparatus was certified by the state in 1985. Since the beginning of operation, there have been 349 research results and 52 of these have received awards of the ministerial level or higher.

In order to ensure the success of the physics experiments, workers have improved the container wall conditions for plasma generation, the heating facility, the power supply control system, and the diagnostic system. They developed a number of diagnostic systems and accepted two projects from the International Atomic Energy Organization: multichannel soft x-ray tomography and measurement of plasma current density by lithium beam. The results were satisfactory. In their effort to improve

Researchers of the Southwest Physics Institute Measuring Vacuum Chamber Parameters of the HL-1

the polar field and the associated power supply system, they employed the copper shell equilibrium feedback technology, the group discharge method and the graphite aperture and titanium evaporation technique. With extensive experimental results and physical analysis, the standard of the physical parameters of the plasma has improved considerably and reached the international level. These results are the basis of China's future fusion-fission hybrid reactors.

Experts from more than 30 universities and research units believe that the physical experimental research results obtained on the No. 1 circulator marked a new milestone in China's controlled fusion research. Novel research by the Southwest Physics Institute on the boundary property and magnetohydrodynamic behavior of plasma has created favorable conditions for China to participate in the international competition in controlled fusion.

Studies of Raman Free Electron Laser by Optical Klystron Configuration

916A0005A Beijing WULI XUEBAO [ACTA PHYSICA SINICA] in Chinese Vol 39 No 9, Sep 90 pp 1379-1384

[Article by Chen Jizhong [7115 1015 1813], Wang Mingchang [3769 2494 7022], Wang Zhijiang [3769 0037 3068], and Lu Zaitong [7120 6528 6639] of Shanghai Institute of Optics and Fine Mechanics of the Chinese Academy of Sciences: "Studies of Raman Free Electron Laser by Optical Klystron Configuration"]

[Abstract] An overall experimental design to study Raman free electron laser with an optical klystron configuration is presented. A one-dimensional single particle model was used to study ways to improve the gain and efficiency of such a free electron laser.

The model involves the use of one-dimensional equations of motion for electrons and includes the calculation of spontaneous radiation power of electrons. Based on the model, the gain and efficiency of the optical klystron as a function of radiation power input P_{in} and axial distance z were obtained. These results are in good agreement with recent experimental data.

It was found that under a given electron beam and oscillating magnetic field, it is possible to simultaneously achieve high gain and high efficiency by adjusting the optical klystron parameters. This behavior may not be very effective for raman free electron lasers operating in the high gain region because near saturation power output may be obtained by varying parameters such as oscillating magnetic field strength and length. However, for a Compton free electron laser operating at a lower frequency (infrared or below), the use of an optical klystron may be an effective way to improve both gain and efficiency.

Design, Construction of BES Main Drift Chamber of BEPC

91FE0057A Beijing GAONENG WULI YU HE WULI [HIGH-ENERGY PHYSICS AND NUCLEAR PHYSICS] in Chinese Vol 14 No 9, Sep 90 pp 777-787 [MS received 22 Nov 89]

[Article by Ma Jimao [7456 1015 5399], Mao Huishun [3029 1979 7311], Bai Jingzhi [4101 2529 5347], Xie Peipei [6200 0160 0160], et al. of CAS Institute of High Energy Physics: "Design, Construction of BES Main Drift Chamber of BEPC"]

[Text] **Abstract**

The physical design, mechanical design and construction, selection of working gas and modeling experiments associated with the main drift chamber of the Beijing-Spectrometer (BES) are briefly described. The experimental or estimated values of various parameters of the main chamber, including solid angle coverage, gain and efficiency, spatial resolution on the R-φ plane, axial spatial resolution, dE/dx energy resolution and particle identification power, are given.

I. Introduction

The large general purpose Beijing Spectrometer (BES) operates on the Beijing Electron Positron Collider (BEPC). Its physical objective is to reconstruct all final states of the high energy e^+e^- reaction. A large-scale precision cylindrical drift chamber, the main drift chamber located at the center of the spectrometer, is responsible for measuring the track, momentum and energy loss dE/dx of charged particles. The main drift chamber has a large solid angle, high detection efficiency, good spatial resolution and momentum resolution, good dE/dx resolution for particle identification, ease of pattern recognition and long operating life. This paper briefly describes the physical design, mechanical design and construction, choice of operating gas, modeling experiment, performance specification and preliminary collision experiment results.

II. Physical Design of Main Drift Chamber

The main drift chamber has an inner diameter of 31 cm, outer diameter of 2.3 m, total length of 3.38 m and axial filament length of 2.12 m. It consists of 10 concentric filament layers, including five axial filament layers and five oblique filament layers to measure particle track on the R-φ and R-θ plane, respectively. The number of elements per layer varies from 48-108. The total number of elements is 702. Each element has four sensing filaments which serve as signal output leads. There are 2,808 filaments in total. In addition, there are a number of auxiliary filaments, making the total number of filaments 19,380. Figure 1 shows a schematic diagram of the structure of the main drift chamber.

1. Element Structure

The design of the main drift chamber is based on a number of sensing filament elements (see Figure 2(a)). Four sensing filaments are placed axially in the element at a spacing of 1 cm apart. Their signals are not only used to measure drift time (track position) but also charge (dE/dx). In order to distinguish track going to the left from that going to the right, sensing filaments are displaced by 350 μm relative to the plane of the center filament. Potential filaments are added between the sensing filaments to minimize signal interference and static deviation. Moreover, gain can be effectively controlled. In order to improve the uniformity of the electric field in the edge of the element, protective filaments are placed at both ends of the center filament plane. The electric field filament forms the boundary of the element. The spacing is 5 mm. The distance between the electric field filament plane to the center filament plane is the half-width of the element, which is the maximum drift distance for an electron. In reality, an element is shaped like a wedge. Its nominal half-width is the half-width at the center of its radius. It is 1.4 cm for layer I, 1.9 cm for layers II and III, 3.1 cm for layers IV-X. Inner layers are smaller in order to minimize the probability of multiple impact. The maximum half-width of the outer element is limited by the spatial resolution requirement. It is primarily determined by electron diffusion effect. Various filament parameters are shown in Figure 2(a).

The above element structure has the following characteristics. The electric field is distributed uniformly. It is possible to accurately use the relation between linear drift distance S and drift time T to provide good spatial resolution, uniform dE/dx sampling and fast pattern recognition. The displacement of sensing filament can be used to determine whether the track in the element is going right or left to accelerate the process. To distinguish right from left, a minimum of three sensing filaments are required. Four is more appropriate to allow some degree of failure. Sensing filament signals in an element are correlated to time. Background and interference can be effectively eliminated. They are usually triggered by one filament, and rarely by three or four filaments. A multiple sensing filament element has the disadvantage of having an inductive pulse in the reverse direction on neighboring filaments during an avalanche. It is equivalent to some correlated noise to make the resolution of the chamber worse. By adding a resistively coupled network between sensing elements, a portion of the original signal is led to neighboring filaments to compensate for the induction signal. This can lower the correlation down to below 1 percent so that it would not affect the result.

2. Layer Structure

Out of the 10 filament layers in the main drift chamber, five are oblique layers. Their arrangement with respect to the coaxial filament layers is shown in Figure 1. A represents an axial filament layer. U and V represent oblique layers in the positive and negative direction, respectively. Since the multiplicity number of final state particles of BES is not large ($\bar{n}_c \simeq 4$), the z-axis of the track is measured by oblique filaments. Compared to the charge distribution method, oblique filament method does not need linear readout electronics. Its gas gain requirement is compatible with that for dE/dx measurement. Furthermore, its position accuracy is even better. Considering pattern recognition and track fitting, it is best to have half and half axial and oblique layers. It is coordinated by a four-layer axial sensing filament in the center drift chamber (a small cylindrical chamber) inside the main drift chamber. Layer I in the main chamber is an oblique filament layer which is used to measure particles with small emission polar angles. It is followed by an axial layer and then an oblique layer in an alternating manner. In addition, the direction of every

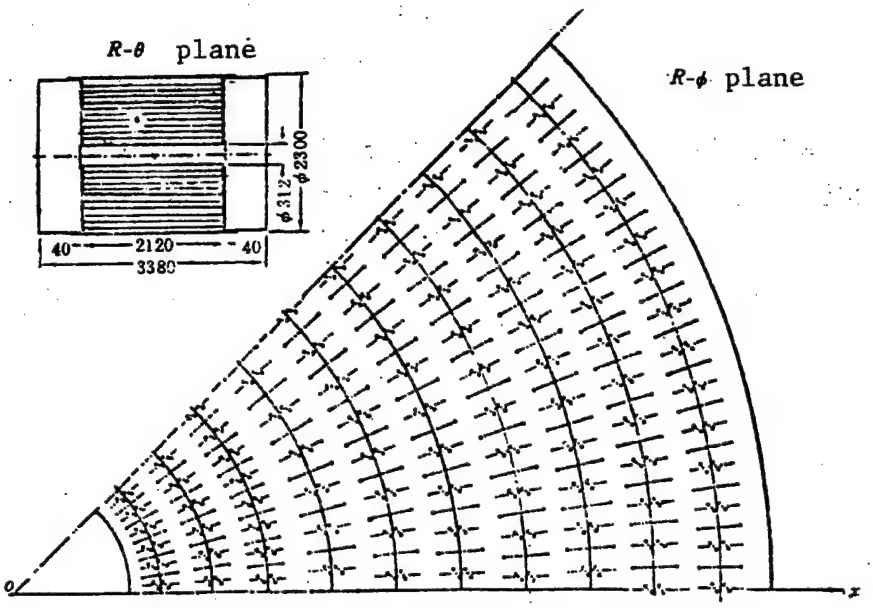

Layer number (filament direction) I(U) II(A) III(V) IV(A) V(U) VI(A) VII(V) VIII(A) IX(U) X(A)

Layer number (filament direction)	I(U)	II(A)	III(V)	IV(A)	V(U)	VI(A)	VII(V)	VIII(A)	IX(U)	X(A)
Center radius (mm)	215	295	375	475	575	675	775	875	975	1075
Elements per layer	48	48	60	48	58	68	78	88	98	108
Element half-width (mm)	14.1	19.3	19.6	31.1	31.1	31.2	31.2	31.2	31.2	31.2
Relative to origin of x-axis	0° (first electric field filament array)	0° (same as I)	0° (same as I)	0° (same as I)	2° (first sensing filament array)	2° (same as V)	5° (second sensing filament array)	5° (same as VII)	0° (first sensing filament array)	0° (same as IX)

Figure 1. Schematic Diagram and Some Parameters of the Main Drift Chamber

oblique layer is reversed. The oblique layers form a revolving hyperboloid. When the angle of inclination of the oblique filament is large, resolution in the z-direction is very high. However, the center plane of the filaments also concaves downward more. This would interfere with the electrostatic structure of the neighboring layer. As a compromise, the range of inclination angle is chosen to be 2.3°-5.0°.

The distance between layers is 3-4 cm. Trigger circuit and track resolution requirements are met by arranging the elements along the orientation angle φ. The first four layers participate in the triggering. Their first electric field filaments are lined up at the x-axis. By matching the number of elements in each layer, a 30° cyclic element arrangement pattern on the R-φ plane can be controlled. This symmetry simplifies the design and construction of

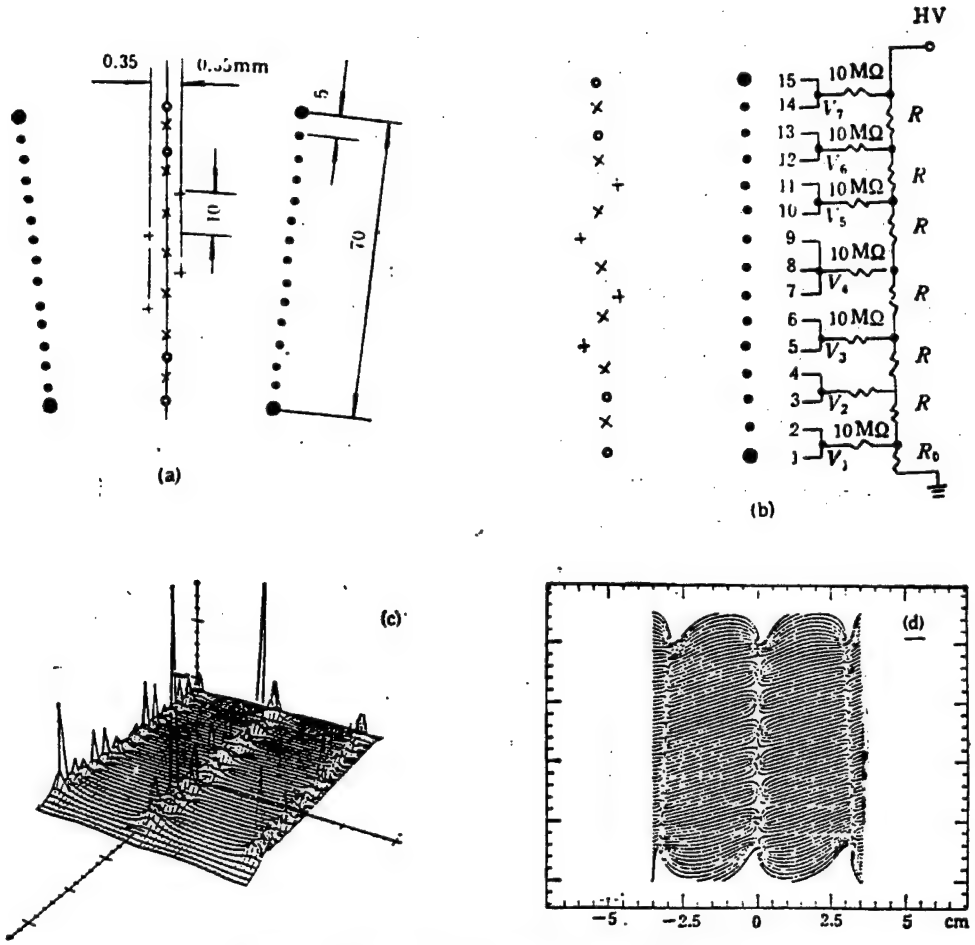

Figure 2. Main Drift Chamber Element Structure

Key:(a) Element structure and parameters: +—sensing filament, 30 μm diameter gold-plated tungsten wire, tension 100 g; x—potential filament, 100 μm diameter gold-plated Fe-Ni-Cr wire, tension 500 g; o—protective filament, 100 μm diameter gold-plated Fe-Ni-Cr wire, tension 500 g; small filled circle—electric field filament, 178 μm diameter gold-plated Be-Cu wire, tension 500 g; large filled circle—thick field filament, 220 μm diameter gold-plated Be-Cu wire, tension 600 g. (b) Schematic of power supply for electric field filaments. (c) Electric field distribution in the element. (d) Electron drift track with applied magnetic field.

the triggering circuit. The remaining six layers do not participate in triggering. The starting points of these layers are offset at the x-axis. An orderless cross pattern between layers is naturally formed by different number of elements. This orderless arrangement prevents a large momentum track from going too close to a filament when pass from the center outward to lower the spatial resolution.

3. Electrostatic Calculation

Electrostatic calculation is a major basis for drift chamber design. The standard for main drift chamber design is that the gain on all sensing filament is M = 5 x 10^4 +/- (10 percent). When using $Ar/CO_2/CH_4$ as the operating gas, it is equivalent to having a filament charge density q = 0.28 +/- (0.5 percent) kV. In most areas in an element (except near a filament), the electric field is E = 0.85 +/- (2 percent) kV/cm. The collection width of dE/dx measurement of the sensing filament Δy may differ by approximately 10 percent due to factors such as filament displacement, edge effect, inter-layer interference, and magnetic field effect. The surface electric field E_s of the edge electric field filament is less than the critical breakdown level.

Electrostatic calculation of the main drift chamber was done using the matrix capacitance program developed by SLAC[2] in the United States. A simplified model involving three layers and nine elements (three elements/layer) was chosen for computation. Results were obtained for the element at the center. Inner and outer

wall were considered as densely populated filaments. In order to simplify the voltage distribution, power was supplied to the wedge element in a special way, i.e., from low to high in the manner of an arithmetic progression (see Figure 2(b)). Effects such as offset in the φ-direction of elements in different layers and a concave oblique filament plane are taken into consideration. Electrostatic calculation provided a series of operating voltage parameters and expected results. Figure 2(c) shows the electric field distribution inside an element. Figure 2(d) shows the electron drift track with an applied electric field. The results can be summarized as follows: a) In layers I-III, each element only needs two protection filaments (on both ends of the center filament plane) to meet the requirements for filament charge density q and electric field strength E. b) In layers IV-X, each element needs four protection filaments to satisfy the requirements. c) These conclusions are not affected by inter-layer offset in the φ-direction and by radial movement of the oblique filament plane. d) Δy, dE/dx collection width, varies with relative element position between layers. In most areas, it is within 10 percent. Local correction may be required. e) When the diameter of edge field filament is 220 μm, its surface electric field strength will not cause breakdown. Because approximation was used in electrostatic calculation, its results must be confirmed by similar modeling experiments.

III. Selection of Operating Gas

The operating gas in the main drift chamber must meet a variety of requirements, including high gas amplifying coefficient, high electron drift velocity and low electric field to reach the saturated drift velocity, small magnetic deflection angle, low electron diffusion coefficient, large particle energy loss dE/dx, and long operating life. In China, the source of such gas limits the selection for a large chamber. Fortunately, a great deal of measurements done by us and by other laboratories abroad[3-5] proved that tertiary gas mixture $Ar/CO_2/CH_4$ = 89 percent/10 percent/1 percent meets all the requirements, especially the most important factor—long operating life. Ar, CO_2, and CH_4 are easily available and relatively cheap in China.

Data relevant to the operating gas $Ar/CO_2/CH_4$ are as follows: gas amplifying factor M is high, saturated drift velocity V_{dr} = 5 cm/μs, electric field to reach saturated drift velocity E_c = 700 V/cm, magnetic deflection angle α_{dr} = 17° (B = 4.1 kG) and 18.9° (B = 4.5 kG), effective diffusion coefficient D ≃ 100 μm/square root of cm, most probable energy loss of smallest ionized particle dE/dx ≃ 1.37 keV/cm, and chamber lifetime is long. When the integrated charge of a unit length of sensing filament is $Q_s \simeq 10^{20}$ electrons, the major performance parameters of the chamber do not change significantly.

IV. Mechanical Design and Construction of the Main Drift Chamber

The main drift chamber is a large thin-wall precision cylindrical structure. Foreign experience with similar drift chambers was used as a reference in its mechanical design. Further modification was also made. The main chamber primarily includes the inner and outer cylinders and the two end plates. Twelve large windows were opened on the 1 cm thick aluminum outer cylinder for pulling the filaments. Afterward, they were covered with thick aluminum shutters. With ensured strength and rigidity, the inner cylinder is a 2 mm thick carbon fiberglass cylinder to minimize multiple Coulombic scattering. The wall mass thickness is 9×10^{-3} r.l. The two aluminum end plates are 4 cm thick. Each plate was machined with 19,380 high precision (similar to 50 μm) 4 mm diameter positioning holes. Insulating locators made of Delrin are inserted in these holes (see Figure 3). Each filament is secured to the fine copper tube at the center of the locator. The total filament tension is 8.7 tons. The two end plates are fixed tightly against the "stops" on the inside of the outer cylinder. One of the end plates is connected to the inner cylinder in a fixed manner and the other in a sliding manner. The pressure on the inner cylinder can be controlled by adjusting the relative position of the end plates. Based on the 200 μm spatial resolution requirement, very high precision machining and assembly are necessary. The nearly 40,000 locator holes on the two end plates were machined by a large precision digital machine tool. Assembly was done under the guidance of a precision optical system. The overall filament positioning accuracy is 80 μm. In order to ensure the reliability of the structure of the main chamber, a system analysis was done using the SAP5 program developed in the United States with a finite element method.[6] Inner and outer cylinders and end plates are plate elements, "stop" ring and reinforcing beam ring are beam elements, support columns are truss elements, connections between end plates and inner and outer cylinders are pseudo-elements, and support for the simulation chamber is a boundary element. In addition, a great deal of boundary elements are used to monitor the accuracy of the calculation. Taking advantage of the symmetry of the main chamber, one-fourth of the structure is divided into 743 nodal points, consisting of five kinds of elements including 528 plate elements, 66 beam elements, 12 truss elements, 51 boundary elements, and 20 pseudo-elements. Furthermore, automatic nodal point generation system and automatic element generation system were fully utilized. On the basis of overall structure computation, further calculations of important local strength such as inner and outer cylinder and end plates were also made. The results showed that both strength and stability of the main chamber meet the design requirement. In addition, it also has good rigidity.

Filaments were pulled using the conventional heavy load welding method in a special ultra-clean room under controlled temperature and humidity. All filaments underwent repeated tension and high voltage tests. In order to prevent the distortion of end plates in the process, a pre-stress technique was successfully applied to ensure the uniformity of filament tension. Since the main chamber was put in operation over a year ago,

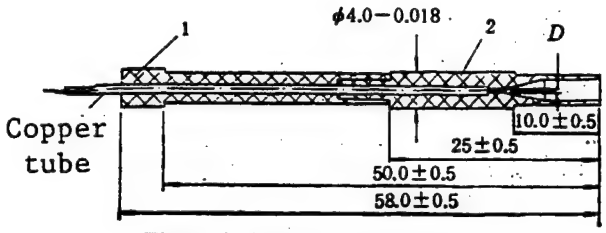

Figure 3. Structure of Locator
D = 190 μm (with respect to signal wire); D = 250 μm (with respect to other wires)

except some auxiliary filaments were pulled out in the early stage, no new broken filaments were found among nearly 20,000 filaments. The main chamber seal works well. Under flow condition, the relative leak rate is 0.3 percent/hour at 10 times over-pressure. Therefore, it is ensured that the gas usage rate is approximately 1 chamber volume/day.

V. Modeling Experiment

The objective of the modeling experiment is to verify the reliability of the physical and mechanical design of the drift chamber in order to make the necessary correction. It also includes studying and solving key technical problems in the construction of the chamber, such as precision machining and assembly of the chamber, filament pulling and replacement technique, fabrication of the insulating locators, arrangement of the high voltage distribution system and signal cables, etc.

The main drift chamber models[7] studied include the modified 22.5° MARK III model, 2.3 m long element model, multi-layer multi-element model and various other experimental apparatus. They were used to measure and analyze individual or overall problems to provide reliable basis for the optimum design and construction scheme. Some experimental results and construction experience have general applications in similar type of work elsewhere.

VI. Performance of Main Drift Chamber

Before installing the spectrometer, output signals from all 2,808 sensing filaments in the main chamber were monitored using cosmic ray. Various performance parameters were measured using the readout electronics in the system.[8] Parameters not directly measured are also estimated here.

1. Solid Angle Coverage

The solid angle Ω for the reception of particle from the point of collision for the cylindrical drift chamber is

$$\Omega = 4\pi L/\sqrt{R^2 + L^2} = 4\pi\cos\theta, \quad (1)$$

where L is the half length of the chamber, R is the emergent radius of the particle and θ is the polar angle with respect to R. Obviously, Ω depends on the number of measurement points. In the main drift chamber, the solid angle corresponding to particles penetrating layer II is 95 percent x 4π. The number of measurement points is eight. It is 90 percent x 4π for particles penetrating layer IV. The number of measurement points is 16. The solid angle for particles penetrating all 10 layers is approximately 70 percent x 4π and there are 40 measurements.

2. Gain and Efficiency

From electrostatic calculation and modeling, a gas gain of $M \cong 5 \times 10^4$ was chosen. At this point, signals are about 25 percent locally saturated and a correction must be made for dE/dx measurement.

With a suitable operating voltage and discriminating threshold, the mean single filament efficiency η = 97 percent, as shown in Figure 4. The corresponding threshold (converted to input of pre-amplifier) is 300 μV. Figure 4(a) shows the number of filaments hit by each track. A fully efficient track should hit 80 filaments. Due to factors such as noise, when a track hits more than 80 in the calculation, it is treated as 80.

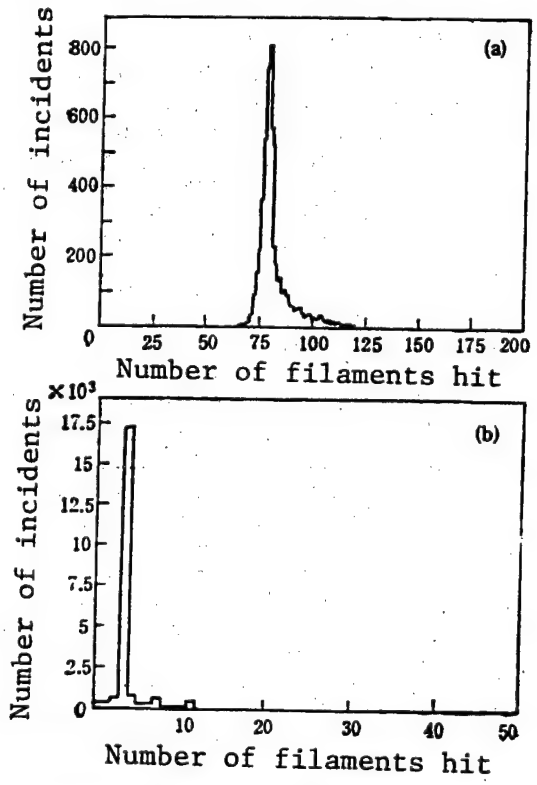

Figure 4. Efficiency of Main Drift Chamber
(a) Distribution of number of filaments hit by a single track; (b) Distribution of number of filaments hit in a layer, total efficiency is 4.

3. Spatial Resolution of the Chamber on the R- Plane

The accuracy of position in the radial direction R is determined by the filament location, which is approximately 80 μm. Figure 5(a) shows the spatial resolution distribution σ_x for a single filament in the direction of orientation angle φ in the cosmic ray experiment. The value for each filament is average of the entire length of the filament and half drift distance of the element. Because of differences in half-width, axial and oblique direction for elements in various layers, σ_x is somewhat different. However, it is between 180-224 μm. Figure 5(b) shows an example using a three-filament method to distinguish right from left in an element and its single filament resolution. The abscissa is $\Delta t = [(t_1 + t_3)/2 - t_2]$ where t_1, t_2, and t_3 are the drift times recorded by three neighboring filaments. The ordinate is the track count. The positive and negative peaks represent whether it is to the left or right of the center filament plane. The spatial resolution of a single filament σ_x can be derived from the peak width $\sigma_{\Delta t}$:

$$\sigma_x = \sqrt{\frac{2}{3}}\,\sigma_{\Delta t} \cdot v_{dr}, \qquad (2)$$

where v_{dr} is the electron drift velocity.

4. Axial (z-Direction) Spatial Resolution

Under the approximation of small angle of inclination, the error in z-axis reading using the oblique filament method is derived to be:

$$\sigma_z \simeq (2L/D)\sigma_x \qquad (3)$$

where D is the displacement of one end of the oblique filament along the circumference. Let σ_x = 200 μm. Thus, σ_z ranges from 2.3-5.0 mm in five oblique filament layers. It is better than the resolution using the charge distribution method (1-2 cm).

5. Momentum Resolution

The transverse momentum resolution in the main chamber, (θ = 90°) σ_{pT}/p_T is determined by its spatial resolution and multiple Coulombic scattering of materials inside the chamber.

$$\left(\frac{\sigma_{p_T}}{p_T}\right)^2 = \left(\frac{\sigma_{p_T}}{p_T}\right)^2_{SP} + \left(\frac{\sigma_{p_T}}{p_T}\right)^2_{MS}. \qquad (4)$$

The contribution from spatial resolution σ_x is:

$$\left(\frac{\sigma_{p_T}}{p_T}\right)_{SP} \simeq 3.3 \times 10^3 \frac{\sigma_x(\mathrm{cm})\,p_T(\mathrm{GeV}/c)}{B(\mathrm{kG})\,l^2(\mathrm{cm}^2)}\sqrt{\frac{720}{N+5}}. \qquad (5)$$

where p_T is the transverse momentum of the particle, B is the axial magnetic field strength, l is the radial length of the particle penetrating the chamber, and N is the number of filament hit. N and l are dependent upon the emergent polar angle θ. When B = 4.5 kG and a particle with momentum p_T = 1 GeV/c penetrates all 10 layers (l = 100 cm, N = 20), then $(\sigma_{pT}/p_T) \simeq 0.8$ percent. The contribution from multiple Coulombic scattering is calculated to be $(\sigma_{pT}/p_T)_{MS} \simeq 1.4$ percent. Therefore, the combined expression is:

$$\left(\frac{\sigma_{p_T}}{p_T}\right)^2 \simeq (0.8\%\,p_T)^2 + (1.4\%)^2. \qquad (6)$$

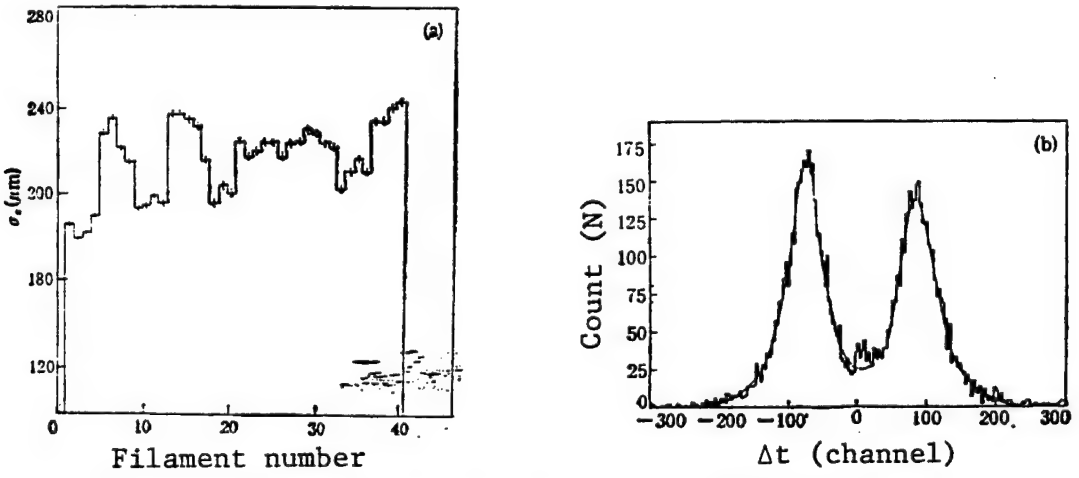

Figure 5. Spatial Resolution in the Main Drift Chamber

(a) Single filament spatial distribution σ_x (layer by layer starting from layer I, each layer with four sensing filaments); (b) Example of single filament resolution using the three-filament method.

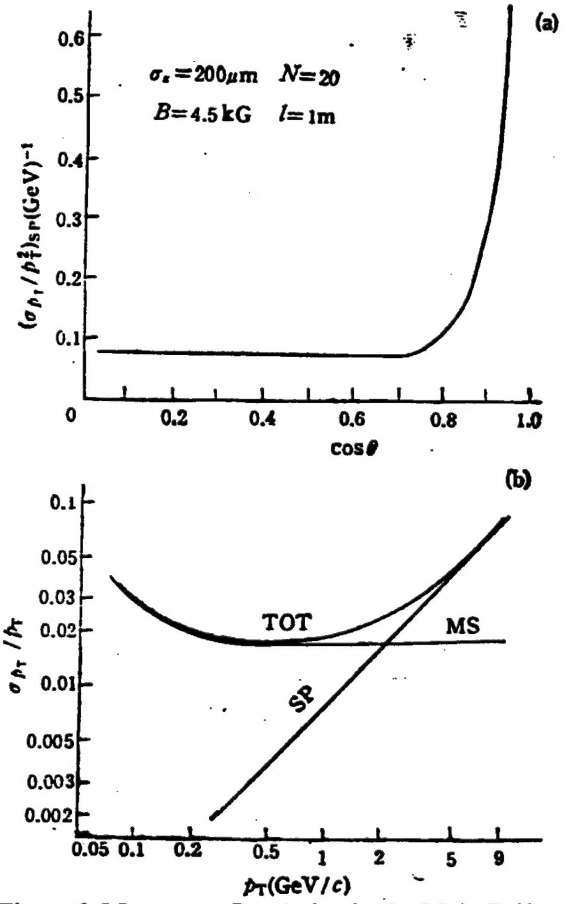

Figure 6. Momentum Resolution in the Main Drift Chamber

(a) $(\sigma_{pT}/p^2_T)_{SP}$ vs. cos θ; (b) σ_{pT}/p^2_T, $(\sigma_{pT}/p_T)_{SP}$, $(\sigma_{pT}/p_T)_{MS}$ vs. p_T.

Figure 6(a) shows the distribution of $(\sigma_{pT}/p_T)_{SP}$ as a function of cosine of the emergent polar angle, cos θ, which also varies with l and N. Figure 6(b) shows σ_{pT}/p_T, including its two components $(\sigma_{pT}/p_T)_{SP}$ and $(\sigma_{pT}/p_T)_{MS}$, as a function of particle momentum. When particle momentum is low, most contribution comes from multiple scattering.

6. Measurement of dE/dx and Particle Identification

By measuring the difference in particle energy loss in the gas dE/dx, an independent particle identification technique was developed. Figure 7(a) shows a typical single filament dE/dx charge spectrum for cosmic ray. It shows that the full width half maximum of its resolution to most probable energy loss ratio, FWHM(1)/E_{mp}, is approximately 100 percent. It is in agreement with the estimate based on a simple model using the smallest ionized particle.[6] If a track is measured N times and the data is treated by a truncated average method, then the energy resolution corrected by the factor $N^{-0.43}$ is:

$$\frac{\sigma_N}{E_{mp}} = \frac{1}{2.35} \cdot \frac{\text{FWHM}(1)}{E_{mp}} N^{-0.43}. \qquad (7)$$

Since N = 40 for the main drift chamber, $\sigma_{40}/E_{mp} \cong 8.7$ percent. Figure 7(b) schematically illustrated this result.

The particle identification power of the main drift chamber is expressed in terms of S which is defined as follows:

$$S = E_i - E_\pi \text{ over } \sigma_\pi,\ i = e, k, p \qquad (8)$$

where E_π and E_i represent the most probable energy losses for particles π and i, respectively. σ_π is the energy resolution power (standard deviation) of π particle with multiple measurements. S represents how many σ_π in energy loss difference for the two particles with the same momentum. Figure 8 shows particle identification power S as a function of momentum p. The momentum limit for different particles separated by 2σ is:

π/K: p ≤ 720 MeV/c,
π/p: p ≤ 1.23 GeV/c,
π/e: p = 0.15 - 10 GeV/c.

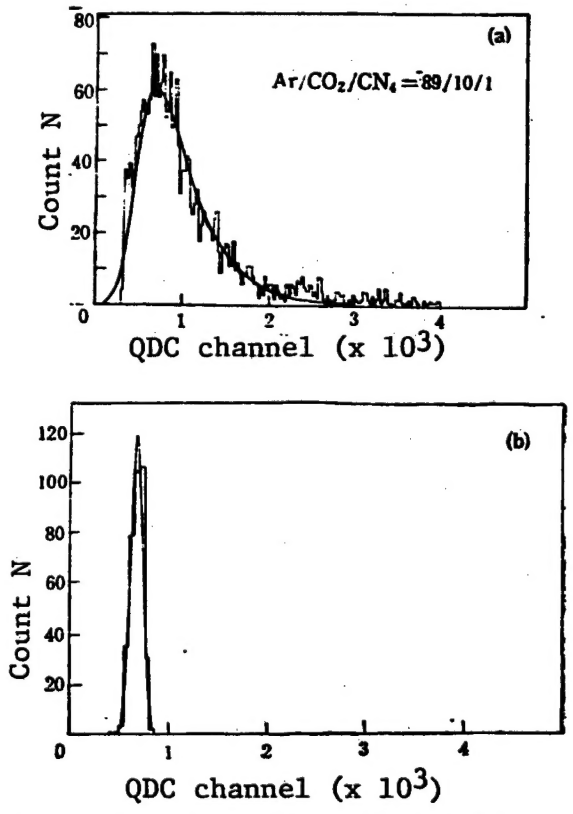

Figure 7. Energy Resolution in Main Drift Chamber

(a) Single filament dE/dx charge spectrum; (b) Truncated average of 40 samples (corresponding to $\sigma_E/E_{mp} \cong 8.7$ percent).

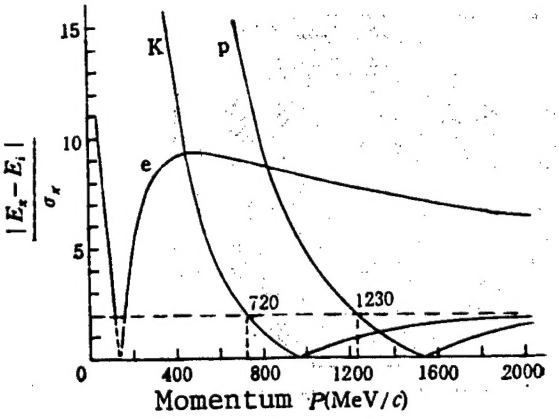

Figure 8. Particle Identification Power vs. Momentum p

The dE/dx method provides good π/K resolution at low momentum and π/e resolution completely independent of shower counter. Complemented by the time of flight method, it satisfies the requirements for BES.

7. Data Quality

Data process is simplified and patter recognition process is accelerated by the uniform electric field, linear S-T relation and left and right recognition in each element. Each layer provides a track vector consisting of close to four filaments on the R-φ plane to be used for direct calculation of track parameters, i.e., radius of curvature ρ of the track and orientation angle φ_0 of the coordinate origin.

$$\rho = \frac{1}{2}\sqrt{R^2 + \left(\frac{dR}{d\phi}\right)^2}, \qquad (9)$$

$$\phi_0 = \phi - \sin^{-1}\left(\frac{R}{2\rho}\right). \qquad (10)$$

where R and φ represent the position of the vector element and $dR/d\varphi$ is the tangent of the vector element which can be measured. The track searching process involves the connection of various vector elements of axial layers. Compared to the conventional multi-point track searching method, it is more efficient. Possible matches in the oblique layers are then found.[10]

VII. Conclusions

BES has been in operation at the first collision point of BEPC for approximately a year. The main drift chamber is stable. Figure 9 shows some typical incidents, including events involving cosmic ray, e^+e^-, and hadron at the J/ψ peak. In these figures, only filaments that were hit are labeled. No correction was made to the drift path. On the R-φ plane, only axial filaments hit represent the particle track. In order to verify its efficiency, oblique filaments hit are also labeled. They are points to the left or right of the track. J/ψ events are still being accumulated on the BES. Millions of $\mu^+\mu^-$ events will be used to evaluate the overall performance of the main chamber.

The development of the main drift chamber is a large project. We wish to express our gratitude to various levels of leadership, factories, and departments and individuals for their assistance in the design, construction, and testing process. In particular, we wish to thank Professor Ye Minghan [0673 6900 3352], Professor A. Seiden, Professor H. F. W. Sadrozinski, Dr. Xu Rongsheng [6079 2827 3932], Dr. G. Hanson, Shi Huanzhang [0670 3562 4545], Deng Shusen [6772 2885 2773], Li Jia [2621 0163], Xu Zhiqing [1776 5365 3237], and people in the drift chamber group of the electronics laboratory.

References

1. Ma Jimao, et al., Main Drift Chamber of BES (two volumes), first draft 1985, revised in 1988-89.

2. H. F. W. Sadrozinski, A. Seiden, and Xu Rongsheng, private communications, 1985. Xu Rongsheng, GAONENG WULI YU HE WULI [HIGH-ENERGY PHYSICS AND NUCLEAR PHYSICS], 10 (1986), 629.

3. Ma Jimao, Mao Zepu [3029 3419 2528], Zhou Jie [0719 2638], and Yan Jie [7346 3381], GAONENG WULI YU HE WULI [HIGH-ENERGY PHYSICS AND NUCLEAR PHYSICS], 9 (1985), 1. Ma Jimao, U. Becker, Ma Daan [7456 1129 1344], and A. H. Walenta, MIT-LNS Technical Report No. 129, 1982.

4. Ma Jimao, Wang Yunyong [3769 6663 3057], Mao Zepu, Xie Peipei, and Yan Jie, GAONENG WULI YU HE WULI [HIGH-ENERGY PHYSICS AND NUCLEAR PHYSICS], 9 (1985), 273.

5. G. Hanson, et al., SLAC-PUB-3317, 3475 (1984).

6. Lei Youyuan [7191 0327 6678] and Li Zengli [2621 2582 0448], Calculation of Structural Strength and Rigidity of the Main Drift Chamber of BES, Information of the Fourth Ministry, 1986. 8.

7. Ma Jimao, Mao Huishun, Bai Jingzhi, Xie Peipei, Yan Jie, et al., Symposium of the Second National Conference on Nuclear Electronics and Nuclear Detectors, 1984. 10; Symposium of the Third National Meeting on Computer Applications in Nuclear Technology, 1985. 10; HE DIANZIXUE YU TANCE JISHU [NUCLEAR ELECTRONICS AND DETECTION TECHNOLOGY], 7 (1987), 247; Symposium of the Third National Conference on Nuclear Electronics and Nuclear Detectors, 1986. 10; GAONENG WULI YU HE WULI [HIGH-ENERGY PHYSICS AND NUCLEAR PHYSICS], 11 (1987), 441.

8. Ma Jimao, Mao Huishun, Bai Jingzhi, Xie Peipei, Yan Jie, et al., GAONENG WULI YU HE WULI [HIGH-ENERGY PHYSICS AND NUCLEAR PHYSICS], 13 (1989), 781.

9. Mao Huishun, GAONENG WULI YU HE WULI [HIGH-ENERGY PHYSICS AND NUCLEAR PHYSICS], 10 (1986), 752.

10. J. Roehrig, et al., SLAC-PUB-3199 (1983).

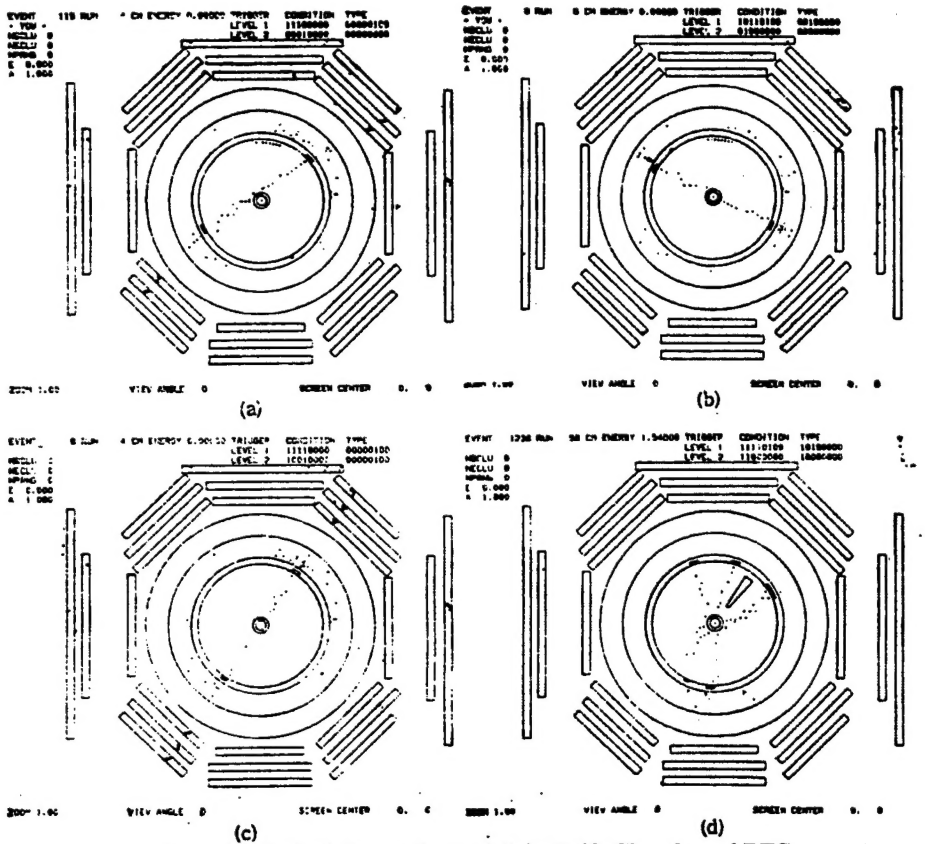

Figure 9. Typical Events in the Main Drift Chamber of BES

(a) cosmic ray; (b) $e^+e^- \rightarrow e^+e^-$; (c) $e^+e^- \rightarrow \mu^+\mu^-$; (d) $e^+e^- \rightarrow$ hadron.

Foreign Broadcast Information Service (FBIS) and Joint Publications Research Service (JPRS) publications contain political, military, economic, environmental, and sociological news, commentary, and other information, as well as scientific and technical data and reports. All information has been obtained from foreign radio and television broadcasts, news agency transmissions, newspapers, books, and periodicals. Items generally are processed from the first or best available sources. It should not be inferred that they have been disseminated only in the medium, in the language, or to the area indicated. Items from foreign language sources are translated; those from English-language sources are transcribed. Except for excluding certain diacritics, FBIS renders personal and place-names in accordance with the romanization systems approved for U.S. Government publications by the U.S. Board of Geographic Names.

Headlines, editorial reports, and material enclosed in brackets [ ] are supplied by FBIS/JPRS. Processing indicators such as [Text] or [Excerpts] in the first line of each item indicate how the information was processed from the original. Unfamiliar names rendered phonetically are enclosed in parentheses. Words or names preceded by a question mark and enclosed in parentheses were not clear from the original source but have been supplied as appropriate to the context. Other unattributed parenthetical notes within the body of an item originate with the source. Times within items are as given by the source. Passages in boldface or italics are as published.

SUBSCRIPTION/PROCUREMENT INFORMATION

The FBIS DAILY REPORT contains current news and information and is published Monday through Friday in eight volumes: China, East Europe, Soviet Union, East Asia, Near East & South Asia, Sub-Saharan Africa, Latin America, and West Europe. Supplements to the DAILY REPORTs may also be available periodically and will be distributed to regular DAILY REPORT subscribers. JPRS publications, which include approximately 50 regional, worldwide, and topical reports, generally contain less time-sensitive information and are published periodically.

Current DAILY REPORTs and JPRS publications are listed in *Government Reports Announcements* issued semimonthly by the National Technical Information Service (NTIS), 5285 Port Royal Road, Springfield, Virginia 22161 and the *Monthly Catalog of U.S. Government Publications* issued by the Superintendent of Documents, U.S. Government Printing Office, Washington, D.C. 20402.

The public may subscribe to either hardcover or microfiche versions of the DAILY REPORTs and JPRS publications through NTIS at the above address or by calling (703) 487-4630. Subscription rates will be provided by NTIS upon request. Subscriptions are available outside the United States from NTIS or appointed foreign dealers. New subscribers should expect a 30-day delay in receipt of the first issue.

U.S. Government offices may obtain subscriptions to the DAILY REPORTs or JPRS publications (hardcover or microfiche) at no charge through their sponsoring organizations. For additional information or assistance, call FBIS, (202) 338-6735,or write to P.O. Box 2604, Washington, D.C. 20013. Department of Defense consumers are required to submit requests through appropriate command validation channels to DIA, RTS-2C, Washington, D.C. 20301. (Telephone: (202) 373-3771, Autovon: 243-3771.)

Back issues or single copies of the DAILY REPORTs and JPRS publications are not available. Both the DAILY REPORTs and the JPRS publications are on file for public reference at the Library of Congress and at many Federal Depository Libraries. Reference copies may also be seen at many public and university libraries throughout the United States.